

Modular Tunable Coupler for Superconducting Circuits


Daniel L. Campbell,^{1,*} Archana Kamal², Leonardo Ranzani³, Michael Senatore^{1,4} and Matthew D. LaHaye^{1,†}

¹*Air Force Research Laboratory, Information Directorate, Rome, New York 13441, USA*

²*Department of Physics and Applied Physics, University of Massachusetts, Lowell, Massachusetts 01854, USA*

³*Raytheon BBN Technologies, Cambridge, Massachusetts 02138, USA*

⁴*Department of Physics, Syracuse University, Syracuse, New York 13244-1130, USA*

 (Received 15 July 2022; revised 31 January 2023; accepted 12 May 2023; published 13 June 2023)

The development of modular and versatile quantum interconnect hardware is a key next step in the scaling of quantum information platforms to larger size and greater functionality. For superconducting quantum systems, fast and well-controlled tunable circuit couplers will be paramount for achieving high-fidelity and resource-efficient connectivity, whether for performing two-qubit gate operations, encoding or decoding a quantum data bus, or interfacing across modalities. Here we propose a versatile and internally tunable double-transmon coupler (DTC) architecture that implements tunable coupling via flux-controlled interference in a three-junction dc superconducting quantum interference device. Crucially, the DTC possesses an internally defined zero-coupling state that is independent of the coupled data qubits or circuit resonators. This makes it particularly attractive as a modular and versatile design element for realizing fast and robust linear coupling in several applications such as high-fidelity two-qubit gate operations, qubit readout, and quantum bus interfacing.

DOI: [10.1103/PhysRevApplied.19.064043](https://doi.org/10.1103/PhysRevApplied.19.064043)

I. INTRODUCTION

Recently, several demonstrations of noisy intermediate-scale quantum (NISQ) processors involving complex systems comprising tens of coupled qubits, have cemented superconducting circuits as a leading platform for large-scale quantum processing [1–5]. Further scaling of quantum processors and the development of distributed quantum architectures will likely benefit from reconfigurable qubit connectivity, tunable dispersive readout, bus interfacing, and transducer interconnects. For all these functionalities the use of a standalone circuit interconnect, a coupler, helps to preserve the coherence of the interconnected circuits while enabling rapid, high-fidelity entangling operations between them.

Tunable couplers use an external control parameter to turn on and off an effective coupling g_{eff} . In superconducting circuits threading flux through a superconducting quantum interference device (SQUID) and applying microwave

driving fields are examples of external control parameters. We highlight two broad approaches to tunable coupling: (i) couplers that use current-divider circuit elements [6–15] (a recent well-known example is the *gmon* coupler [11,12]), and (ii) couplers that interfere direct and virtual interaction pathways [16–26], such as the single-transmon coupler [16–22]. For the latter case, mutual inductance or capacitance between two qubits constitutes a direct interaction pathway while interactions mediated by coupler circuitry constitute a virtual interaction pathway. Between these two coupling approaches, current divider couplers respond more linearly with flux, lending themselves to parametric coupling applications [13,15,27]. On the other hand, inductively connecting the qubits introduces extra flux degrees of freedom, which, by extension, leads to additional noise and decoherence channels, and crosstalk between local flux-bias lines. A survey of coupler modalities cited in this paper, therefore, suggests that capacitive interactions lead to cleaner and potentially easier-to-control circuitry. Moreover, for circuit-QED architectures involving transmon qubits, capacitive interactions are compatible with the fixed-frequency designs routinely employed in high-coherence circuits. Therefore, on balance, capacitive rather than inductive coupling seems to provide a significant advantage for the interference- over current divider-style coupler modality especially for multiqubit superconducting systems.

*Daniel.Campbell.22@us.af.mil

†Matthew.LaHaye@us.af.mil

Published by the American Physical Society under the terms of the [Creative Commons Attribution 4.0 International](https://creativecommons.org/licenses/by/4.0/) license. Further distribution of this work must maintain attribution to the author(s) and the published article's title, journal citation, and DOI.

It is worthwhile to note that in the highlighted coupler approaches, the frequencies of the qubits and the magnitude of their interaction with the coupler determine the decoupling external flux bias $\Phi_e^{(0)}$ that zeroes the qubit-qubit effective coupling $g_{\text{eff}} = 0$; this necessitates circuit remodeling and optimization each time data qubits or architecture is even slightly modified. In addition, the quantum level structure of an interference coupler makes the realization of parametrically driven exchange interactions challenging, an increasingly critical functionality explored in several demonstrations [28–30]. Motivated by these considerations several workarounds for parametric coupling, which do not involve modulating the transition frequency of the coupler itself, are gaining traction, such as modulation of the data-qubit frequency itself in the presence of a fixed coupling [31–34] and techniques that do not use flux driving [7,35,36].

In this paper, we describe and analyze a double-transmon coupler (DTC) design, also explored in Refs. [37, 38], that provides the linearity to implement two-qubit parametric gates efficiently and possesses an internally defined zero-coupling state that is independent of the coupled data qubits or circuit resonators. Furthermore, we introduce computationally friendly numerics and analytical expressions for the effective coupling of this circuit, as well as provide theoretical predictions for parametric

and waveguide coupling use cases that are unique to this work.

The DTC uses two inductively coupled transmon qubits to combine the linearity of current divider couplers with the capacitive coupler-qubit interactions of interference-style couplers at the cost of added level structure. From this combination of attributes, we predict fast, linear, and low-noise tunable coupling for the DTC that is compatible with both fixed-frequency transmon architectures and parametric coupling use cases. The design paradigm works on a simple principle: each qubit capacitively interacts with a different transmon belonging to the coupler, as illustrated in Figs. 1(a) and 1(b). These two coupler transmons in turn hybridize with an interaction that can be flux tuned from negative to positive values. The qubits thus virtually interact via simultaneous coupling to the same hybridized states. Moreover, this net virtual interaction between the qubits can be turned off by flux tuning the coupler transmon interaction and hybridization to zero.

Crucially, the addition of a second interposing transmon in the DTC compared to the interference approach suppresses the effective capacitance coupling between data qubits. The suppression geometrically scales with each interposing coupler transmon in the dispersive limit. By controllably hybridizing the DTC's transmons, effective coupling comparable to that of a single interposing

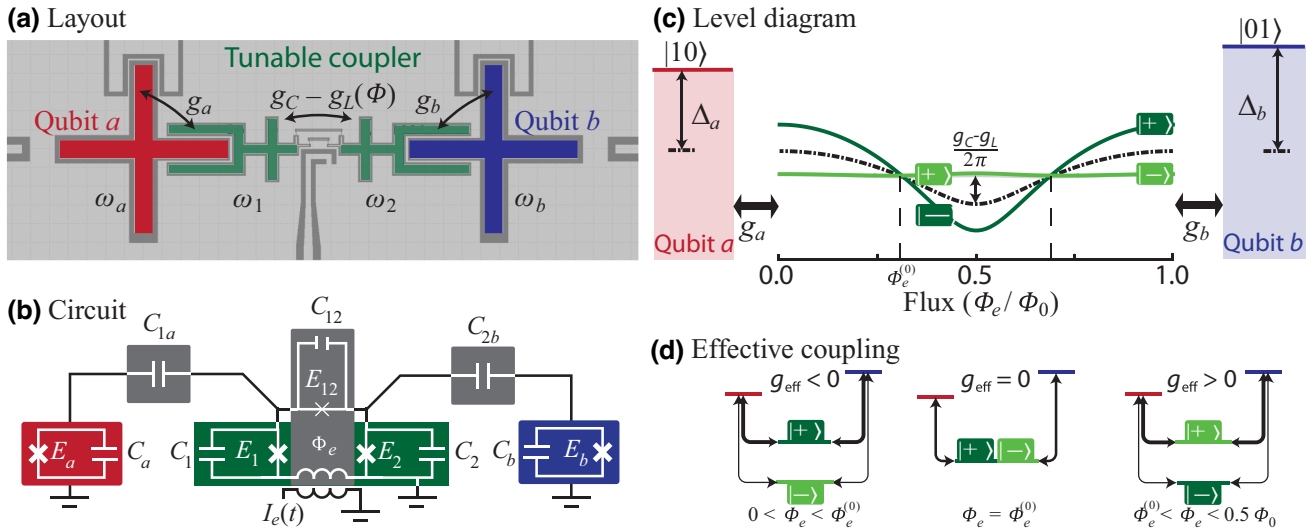


FIG. 1. (a) Prospective device layout. The coupler consists of a pair of transmon circuits (green) coupled by variably strong capacitance g_C and strong flux tunable inductance $g_L(\Phi)$. Each coupler transmon capacitively couples, in turn, to separate qubits (red and blue). $\{\omega_a, \omega_1, \omega_2, \omega_b\}/2\pi$ label transmon plasma frequencies in order of appearance, left to right. (b) The equivalent circuit representation used for the analysis in this work [Appendix A]. (c) A flux-controlled interaction $g_C - g_L$ turns on a hybridization between the coupler transmons. Solid lines represent hybridized coupler eigenenergies ω_{\pm} : the dark and light green lines show ω_{\pm} for capacitive coupling $g_C/2\pi = 0$ and 123 MHz, respectively. Average coupler energy, $\bar{\omega} = (\omega_1 + \omega_2)/2$, is represented with the dashed black line. The detuning of each qubit from the average energy is denoted with the detuning $\Delta_j = \omega_j - \bar{\omega}$ for $j \in \{a, b\}$. (d) Different coupling configurations realized for three distinct flux biases. For simplicity of presentation, we assume $\omega_1 = \omega_2$ (i.e., $\delta = 0$) in (c),(d), for which the magnitude of the interaction between coupler transmons can be directly read off from the splitting between the $|+\rangle$ and $|-\rangle$ eigenstates.

transmon is achievable, while preserving the increased data-qubit isolation. Moreover, the junction and capacitor parameters of the DTC set the functional dependence of the DTC's flux tuning almost exclusively, making the decoupling flux bias $\Phi_e^{(0)}$ depend only weakly on the transition frequencies of the qubits or qubit-DTC interaction strength (if at all). In summary, this *hybridization style* coupler isolates qubits in its "off" configuration and its internal operations are insensitive to the frequencies and use case of the qubits to which it is coupled: a desirable feature of modular design. We also see that the additional transmon degree of freedom in the DTC can be leveraged to realize parametric coupling that mitigates deleterious nonlinear effects, such as rectification in the presence of fast flux modulation.

II. DOUBLE-TRANSMON COUPLER MODEL AND OPERATION

The DTC circuit consists of two superconducting transmon qubits [39] sharing a common ground. The Josephson and charging energies for each transmon are denoted by E_j and E_{Cj} for $j \in \{1, 2\}$. A relatively high inductance junction $E_{12} \sim 0.1 \times E_{1,2}$ connects the two transmons, forming a three junction dc SQUID, see Fig. 1(b). A local bias line with an externally sourced current threads a tunable magnetic field through the SQUID, which tunes the inductive interaction between the transmons,

$$g_L = \frac{4E'_{12}\sqrt{E_{C1}E_{C2}}}{\hbar^2\sqrt{\omega_1\omega_2}}, \quad (1)$$

where $E'_{12} \sim E_{12} \cos(\Phi_e/\varphi_0)$ is the external flux-dependent Josephson energy of the center junction [Appendix A] and $\varphi_0 = \Phi_0/2\pi$ is the reduced flux quantum. The plasma frequencies, $\omega_j = (8(E'_j + E'_{12})E_{Cj})^{1/2}$ also tune modestly with flux through flux dependence of both E'_{12} and $E'_j \sim E_j - E_{12}^2 \sin^2(\Phi_e/\varphi_0)/2E_j$. In contrast, the capacitive interaction between the coupler transmons,

$$g_C \approx \frac{C_{12}\sqrt{\omega_1\omega_2}}{2\sqrt{(C_1 + C_{12})(C_2 + C_{12})}}, \quad (2)$$

remains relatively constant as a function of flux. These inductive and capacitive contributions compete to define the net exchange interaction $g_C - g_L(\Phi_e)$, as shown in Fig. 1(c) [also see Eq. (A6)].

To model and simulate this coupling approach, we now consider a chain of four transmon circuits. The outer transmons operate as data qubits with plasma frequencies $\{\omega_a, \omega_b\}$, while the inner transmons comprise the coupler with plasma frequencies $\{\omega_1, \omega_2\}$. Each qubit capacitively couples to a *different* coupler transmon, with strength g_a and g_b , respectively. The effective coupling between the data qubits may then be understood as a competition

between virtual interactions mediated through the $|+\rangle$ and $|-\rangle$ coupler eigenstates, as shown in Fig. 1(d). This allows tuning g_{eff} from positive to negative values as a nearly linear function of $g_C - g_L(\Phi_e)$, and guarantees the existence of an external flux $\Phi_e^{(0)}$ such that $g_{\text{eff}} = 0$. Anharmonicity in the DTC renormalizes g_{eff} at the 20% level but otherwise the form for g_{eff} and $\Phi_e^{(0)}$ is similar to that of coupled harmonic oscillators with the same connectivity. The equivalent harmonic oscillator Hamiltonian of circuit can then be represented as [see Appendix B],

$$H/\hbar = \sum_{j=a,b,1,2} \omega_j a_j^\dagger a_j + (g_C - g_L(\Phi_e))(a_1^\dagger a_2 + a_1 a_2^\dagger) + g_a(a_a^\dagger a_1 + a_a a_1^\dagger) + g_b(a_b^\dagger a_2 + a_b a_2^\dagger), \quad (3)$$

where a_j^\dagger and a_j are the raising and lowering operators, while the index j identifies the respective qubit $j = \{a, b\}$ or DTC $j = \{1, 2\}$ transmon modes.

To compute g_{eff} we first diagonalize the coupler part of the circuit, yielding $\omega_\pm = \bar{\omega} \pm (\delta^2 + (g_C - g_L)^2)^{1/2}$ where $2\bar{\omega} = \omega_1 + \omega_2$ and $2\delta = \omega_1 - \omega_2$ are the coupler transmon sum and difference plasma frequencies, respectively. Since $\{\omega_1, \omega_2\}$ move together with flux, the common-mode frequency $\bar{\omega}$ also tunes with flux, whereas δ may tune only weakly, if at all. With $\delta = 0$, the modulation of both g_L and $\bar{\omega}$ are nearly equal so that one of the two coupler eigenmode plasma frequencies tunes only weakly with flux, as shown in Fig. 1(c). In the other regime, when $\delta \gg |g_C - g_L|$, both coupler eigenmode plasma frequencies modulate similarly with flux, driven by flux tuning of $\bar{\omega}$.

A. DERIVATION OF THE EFFECTIVE COUPLING

We now consider the data-qubit interaction with the coupler eigenmodes. To gain insight into the nature of the coupler operation, we treat this under the dispersive approximation, i.e., $g_j/|\omega_j - \omega_\pm| < 0.1$, where approximate analytical expression can be derived. To this end, the first step involves perturbatively decoupling the coupler eigenmodes from the qubit modes using Schrieffer-Wolff transformation of the form $U_{\text{SW}} = \exp\left[\sum_\pm \sum_{j=a,b} (g_j/(\omega_j - \omega_\pm))(a_j^\dagger a_\pm - a_j a_\pm^\dagger)\right]$. Retaining terms to second order in $g_j/(\omega_j - \omega_\pm)$, and continuing to omit qubit and DTC anharmonicity, leads to the following effective two-qubit Hamiltonian:

$$\tilde{H}/\hbar \approx \sum_{j=a,b} (\omega_j + \omega_{\text{ac}}^j) a_j^\dagger a_j + g_{\text{eff}} (a_a^\dagger a_b + a_a a_b^\dagger), \quad (4)$$

with a simplified form of the effective qubit-qubit coupling and dispersive shifts on the qubits given by [see

Appendix C],

$$g_{\text{eff}} \approx \sum_{j=a,b} \frac{g_a g_b [(g_C - g_L) + (g_C + g_L)(\Delta_j/\bar{\omega})]}{2D_j^2}, \quad (5)$$

$$\omega_{\text{ac}}^a \approx g_a^2 \left[\frac{\omega_a - \omega_1}{2D_j^2} \right], \quad \omega_{\text{ac}}^b \approx g_b^2 \left[\frac{\omega_b - \omega_2}{2D_j^2} \right], \quad (6)$$

where $D_j^2 = \Delta_j^2 - \delta^2 - (g_C - g_L)^2$. The flux dependence of $\bar{\omega}$, and therefore $\Delta_j = \omega_j - \bar{\omega}$, accounts for the non-sinusoidal tuning with flux shown in Fig. 2. Operating in the regimes where $|\omega_a - \omega_1|, |\omega_b - \omega_2| \gg |g_C - g_L|$ and to a lesser extent when $\delta \gg |g_C - g_L|$ results in more sinusoidal tuning. For the parameters used in figures of this paper, change in ω_{ac}^j with flux is less than or equal to g_{eff} .

The externally applied flux (Φ_e) preferentially drops across the junction E_{12} , which has the highest impedance ($E_{12} \ll E_1, E_2$): E_{12} therefore sets coupler hybridization

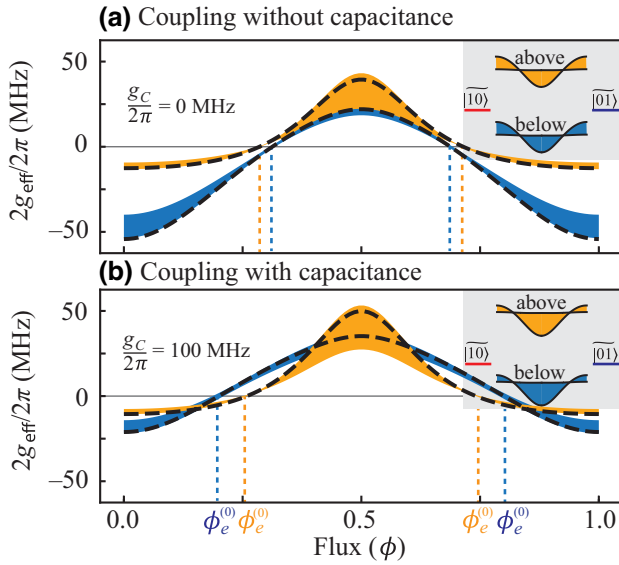


FIG. 2. The $2g_{\text{eff}}$ between degenerate qubits, mediated by the coupler as a function of flux, changes if the coupler transitions are set above versus below the qubit transitions, all else being equal. The shading indicates the standard deviation from the mean after applying 6% relative Gaussian noise on all the coupler junctions, obtained using numerical simulation [Eq. (B15)]. The numerical simulations find $2g_{\text{eff}}/2\pi$ by taking the minimum difference between the eigenfrequencies that best correspond to the states $|1000\rangle$ and $|0001\rangle$ as ω_b is swept past ω_a . A comparison of (a) versus (b) shows that adding capacitance shifts g_{eff} to more positive values. For each scenario, the approximate analytic g_{eff} is plotted in black [Eq. (C23)]. At $\Phi_e^{(0)}$, the coupling parameters are given by $g/2\pi = 0.25$ GHz, $|\Delta|/2\pi = 1.1$ GHz, $\delta \approx 0$, and the qubit plasma frequencies are $\omega/2\pi = 4.7$ GHz. The average junction parameters for (a) are $E_{12}/h = 1.46$ GHz and $E_1/h, E_2/h = 7.5$ GHz, whereas for (b) they are $E_{12}/h = 2.56$ GHz and $E_1/h, E_2/h = 23$ GHz. For all calculations, we choose E_{12}/h to set the maximum inductive coupling to $g_L/2\pi = 0.31$ GHz.

via $g_L(\Phi_e)$. The shunt junctions E_1 and E_2 protect the coupler hybridization from charge noise, interaction with qubits, and other external circuitry. As a consequence, the decoupling flux bias, $\Phi_e^{(0)}$ such that $g_C - g_L(\Phi_e^{(0)}) \propto g_{\text{eff}}(\Phi_e^{(0)}) = 0$, is *internally defined* by the choice of coupler junction parameters. Figure 2 shows $2g_{\text{eff}}$ as a function of flux Φ_e , for two choices of coupler transmon transitions, above (orange) or below (blue) the qubit (blue) transitions. The shaded region shows the gap between the qubit eigenfrequencies, numerically calculated using Eq. (B15), where qubit b is swept into degeneracy with qubit a . These calculations are repeated 30 times with 6% Gaussian random variation applied independently to the three DTC junction parameters: the width of the shading shows the standard deviation in $2g_{\text{eff}}$ at each Φ_e . Note the insensitivity of $\Phi_e^{(0)}$ to variation in the junction parameters. By contrast, increasing g_C shifts $\Phi_e^{(0)}$ further away from $\Phi_e/\Phi_0 = 0.5$ as shown by comparing Figs. 2(a) and 2(b). The analytical expression for g_{eff} [Eq. (C23)] matches numerical simulations to within several percent in the dispersive limit. Equation (C23) contains additional terms that correspond to an approximately 20% correction to Eq. (5).

B. Coupling nearly degenerate qubits

The independence of $\Phi_e^{(0)}$ from the qubit plasma frequency allows for straightforward implementation of degenerate coupling strategies. As an example, consider two qubits, each dispersively coupled to a separate coupler transmon, as shown in Figs. 3(a) and 3(b). To implement a controlled-Z operation, data qubit b is initialized at a frequency ω_b that is 500 MHz higher than ω_a ; having some frequency detuning between the qubits helps to mitigate single-qubit microwave crosstalk. Meanwhile, the DTC flux bias is set to $\Phi_e = \Phi_e^{(0)}$. Next, by tuning the frequency of either qubit, the state $|2000\rangle$ is swept into

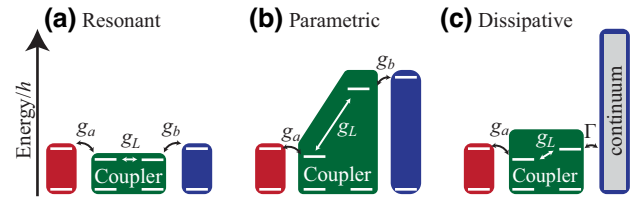


FIG. 3. Quantum state and coupling primitives for resonant, parametric, and dissipative use cases. (a) A static coupling between nearly resonant qubits may be turned on with a static g_L . (b) Parametric coupling between circuit elements with very different transition frequencies may be accomplished by modulating g_L at the frequency difference. The hybridization of coupler transmons modulates even when its transmon plasma frequencies differ. Coupling magnitude scales inversely with the relative detuning of each coupler transmon from its qubit. (c) Purcell decay of a qubit through the coupler is turned off when $g_L = 0$. This functionality allows waveform shaping of qubit emission into a waveguide.

degeneracy with $|1001\rangle$ [Fig. 3(a)], where the kets label transmon modes in Fig. 1(b) from left to right. When the states approach degeneracy, Φ_e is ramped away from $\Phi_e^{(0)}$, turning on a static coupling. The system then evolves for the requisite dwell time at the resulting avoided level crossing. Subsequently, the inverse of the previous flux ramps is implemented to complete the controlled-Z operation [11,16,17,19,20]. Unlike interference couplers [16], $\Phi_e^{(0)}$ remains a constant throughout the procedure, enhancing ease of use. A procedure for using a DTC to implement controlled-Z between nondegenerate fixed-frequency qubits is also explored in Refs. [37,38].

In a similar manner, it is also possible to implement *i*SWAP operations via standard approaches [40] utilizing the DTC SQUID. It should be noted, though, that even for evolution under the effective Hamiltonian in Eq. (4)—as is the case for the DTC—turning on g_{eff} to perform *i*SWAP between $|1000\rangle$ and $|0001\rangle$ likewise turns on parasitic $\sigma_z\sigma_z$ phase evolution from interactions in the second excitation manifold $|0002\rangle \leftrightarrow |1001\rangle$, which must be separately canceled [17,41–43].

The DTC shares features with other three island transmon circuits [44] as well as the capacitively shunted flux (CSFQ) qubit [45]. Like the CSFQ, the anharmonicity of DTC transitions change as Φ_e is swept from zero flux to $0.5\Phi_0$. In the $E_{12} \ll E_1, E_2$ regime, the anharmonicity of the symmetric eigenstate transition of two strongly hybridized transmons $\omega_1 \approx \omega_2$ changes from weakly negative (transmon regime) to near zero. In Fig. 1(c), the eigenenergy of the symmetric eigenstate can be seen to vary with Φ_e , while the small negative anharmonicity of the antisymmetric eigenstate remains constant with Φ_e . The DTC can eliminate both $\sigma_x\sigma_x$ and $\sigma_z\sigma_z$ interactions at the cancellation flux $\Phi_e = \Phi_e^{(0)}$, irrespective of qubit-qubit detuning. While such cancelations can be achieved in interference-based couplers, this necessitates parameter fine tuning and frequency crowding [37].

III. COUPLING WITH A PARAMETRIC DRIVE

We now discuss how the DTC can be employed to implement time-dependent parametric coupling. To this end, a parametric modulation of external flux $\Phi_e = (A \sin(\omega_d t) + 0.25)\Phi_0$ can mediate Rabi-like exchange interactions with rate g_{eff}^p between fixed-frequency qubits (or between other circuit elements) by tuning ω_d at resonance with the difference of relevant transition frequencies [Fig. 3(b)]. The magnitude of resultant parametric coupling g_{eff}^p may be understood in a rotating frame, obtained via the transformation $(a_a^p, a_1^p, a_b^p, a_2^p) = (a_a, a_1, a_b e^{i\omega_d t}, a_2 e^{i\omega_d t})$, where qubits a and b are rendered degenerate by the parametric driving [Fig. 4(a)]. Neglecting the fast rotating terms, the resulting stationary Hamiltonian is manifestly similar to Eq. (3) with effective coupling given by Eq. (5). Substituting $\omega_2^p = \omega_2 - \omega_d$, $\omega_b^p = \omega_b -$

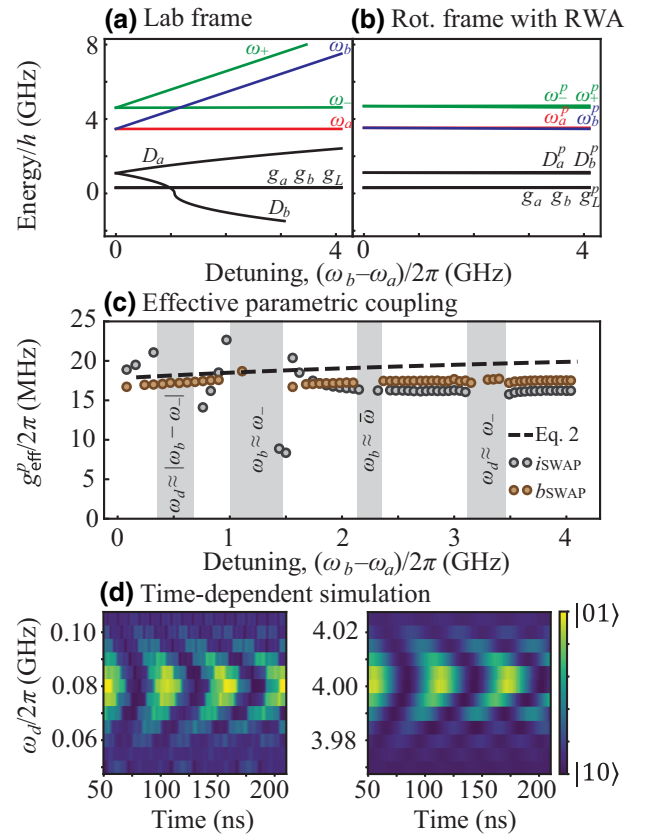


FIG. 4. Model parameters as a function of data transmon detuning defined in the (a) lab frame and (b) frame rotating with the parametric drive at $\omega_d = \omega_b - \omega_a$, as defined in the main text. The square-root denominator $D_j = \text{sign}(D_j^2) \sqrt{D_j^2}$ competes with the magnitude of g_a, g_b, g_C , and g_L to set the size of g_{eff}^p . (c) The lab-frame parameters are chosen such that the rotating-frame parameters are constant as a function of data-transmon detuning: g_{eff}^p [Eq. (C29)] then also remains constant for *i*SWAP- and *b*SWAP-style exchange interactions. This picture breaks down in the shaded regions where accidental degeneracies arise between the data and coupler transmon transitions. The circular markers are resonant exchange rates obtained from two-dimensional fits to the *i*SWAP or *b*SWAP time-dependent Schrödinger equation (TDSE) simulations [Eq. (B15)] performed for different choices of parametric drive frequency $\omega_d/2\pi$ at fixed qubit-qubit detunings $(\omega_b - \omega_a)/2\pi$. (d) TDSE *i*SWAP simulations with $(\omega_b - \omega_a)/2\pi$ equal to 0.08 GHz and 4.00 GHz are shown in the (left) and (right) panels, respectively. The drive amplitude increases to its maximum value over 50 ns (not shown). The left panel shows substantial contributions from counter-rotating terms.

ω_d , and $\bar{\omega}^p = \bar{\omega} - \omega_d/2$ into $\Delta_j^p = \omega_j^p - \bar{\omega}^p$ and $2\delta_j^p = \omega_1^p - \omega_2^p$ with $g_L^p = (2\pi A - (2\pi A)^3/8)g_L(\Phi_e = 0)$, we obtain the parameters given in Fig. 4(b) and the effective parametric coupling strength as,

$$g_{\text{eff}}^p \approx \sum_{j=a,b} \frac{-g_a g_b g_L^p (1 - \Delta_j^p / \bar{\omega}^p)}{4(D_j^p)^2}, \quad (7)$$

where $(D_j^p)^2 = (\Delta_j^p)^2 - (\delta^p)^2 - (g_L^p)^2/2 - g_c^2$. While the qubit detuning and pump frequency need to be swept in tandem to maintain resonance $\omega_d = \omega_b - \omega_a$, the relative detuning between coupler transmon and qubit can be kept fixed, i.e., $|\omega_a - \omega_1| \sim |\omega_b - \omega_2|$. As a consequence, Δ_j^p and δ_j^p also remain constant in the rotating frame as plotted in Fig. 4(b). Adjusting g_a, g_b , and g_L^p to remain constant as other variables change [Appendix A], g_{eff}^p can be held constant as a function of flux. Under these circumstances numerical simulation confirms a constant g_{eff}^p , as shown in Fig. 4(b), in qualitative agreement with Eq. (7). While numerical simulations include terms up to sixth order in the raising and lowering operators [Fig. 6], the analytical expression in Eq. (7) is derived using a simplified harmonic oscillator model [Eq. (4)] that neglects anharmonicity. However, the expression that generated the dotted line in Fig. 4(c) incorporates small corrections for the anharmonicity [Eq. (C23)]. When the coupling is turned on, numerical simulations show $\sqrt{2}$ stronger coupling within the second-excitation manifold compared to within the first-excitation manifold, qualitatively consistent with the simplified analytical model. The qualitative agreement between this model and numerical simulation implies that the anharmonicity of the coupler transmons does not play a strong role in setting g_{eff} or g_{eff}^p .

Another consideration for parametric coupling is the rectification of data-qubit frequency due to flux modulation. Specifically, ω_{ac}^j of the driven qubits scales inversely with $1/(\omega_j - \omega_{\pm})$, which can change nonlinearly with flux; if the parametric drive periodically brings ω_j close to ω_{\pm} , it can introduce a time-averaged drive amplitude dependence to the Rabi resonance condition that manifests as distortion of the time-domain swap envelope. As shown by the simulations presented in Fig. 4(c), such distortion remains negligible if the coupler-induced time-averaged frequency shifts are less than $0.1 \times g_{\text{eff}}^p$. Relative to interference-based couplers, the DTC mitigates the deleterious impact of the nonlinear flux dependence shifts in two ways. First, the DTC eigenenergies tune gently with effective coupling. Second, the freedom to set the detuning and interaction rate g_j separately for each DTC transmon-qubit pair in fabrication allows the tuning of ω_{ac}^a and ω_{ac}^b with flux to be balanced. This balancing strategy roughly maximizes g_{eff}^p for a fixed magnitude of nonlinearity. The combination of these factors allows straightforward, and relatively fast, pairwise parametric coupling between non-degenerate fixed-frequency qubits, among other applications. The parameters used in Figs. 2 and 4 represent a worst-case scenario for second-order nonlinearity generation, where $\delta \sim 0$. Even so, parametric coupling of qubits with 80-MHz relative detuning showed Rabi-like state evolution, such as that shown in Fig. 4(d), persists as E_{12} increases 10% (1%) for the coupler transitions placed below (above) the qubit transitions.

A parametric drive can also induce unwanted direct energy exchange between various states in the Hilbert space, i.e., $\omega_d \approx |\omega_j - \omega_{\pm}|$, that should be avoided through appropriate choice of coupler transitions in fabrication. This is an important consideration for small qubit detuning. For larger qubit detunings, some driving frequencies will excite the DTC directly $\omega_d \sim \omega_{\pm}$. A weak, undesirable, multiphoton exchange interactions will also occur in the second excited manifold $|1001\rangle \leftrightarrow |0110\rangle$ when $\bar{\omega} = (\omega_a + \omega_b)/2$: choosing the level structure as depicted in Figs. 4 and 3(a) and 3(b) avoids this undesirable degeneracy.

IV. COUPLING TO A WAVEGUIDE

The last use case that we consider is fast tunable coupling between a waveguide (or other open quantum system) and a qubit, as depicted in Fig. 3(c). This use case is thematically consistent with previous demonstrations [28,46]. For this scenario we make the left data qubit and the right DTC transmon degenerate, i.e., $\omega_a = \omega_2$, which invalidates the dispersive approximation used in Eq. (4). Instead, the effective tunable coupling is given by $g_a(g_c - g_L)/2\delta$, which goes to zero when the flux is set to $\Phi_e^{(0)}$. If the degeneracy between the qubit and DTC transmon is broken, the qubit relaxation rate into the waveguide under the dispersive limit is given by $\Gamma g_a^2(g_c - g_L)^2/D_a^4$, which is typically small. Further, for $\omega_a \neq \omega_2$, the use cases described in Figs. 3(b) and 3(c) can be combined to realize strong coupling to a continuum without demanding degeneracy between qubit and DTC transitions.

V. ENERGY RELAXATION AND COHERENCE CONSIDERATIONS

Our DTC layout [Fig. 1(a)] uses a grounded coplanar waveguide with impedance $Z_0 = 50 \Omega$ that is shorted near the three-junction SQUID loop: current in the waveguide induces a controllable flux Φ_e via a mutual inductance M to the loop. The three-junction DTC SQUID allows direct exchange coupling between the DTC states and current excitations in the flux-bias line. Using the circuit model discussed in Appendix D, the resultant uncorrelated relaxation rate of each DTC transmon into the bias line can be approximated as, $\Gamma_{1,j} \approx M^2 E_{12}^2 \cos^2(\Phi_e/\varphi_0)/Z_0 \varphi_0^4 C_j$ for $j \in \{1, 2\}$, which only doubles if g_c is increased from zero to $g_c \sim g_L$: see the expression for ξ_j and the derivation for $\Gamma_{1,j}$ in Appendix D. Therefore, DTCs with small mutual inductive coupling $M \leq 3$ pH likely will not need additional low-pass filters on their current bias lines so long as the thermal population of the flux-bias line is low. Conveniently, Γ_1 also tunes to zero at $g_L = 0$: thus, energy relaxation of the coupler into its flux-bias line occurs only when $g_{\text{eff}} \neq 0$ in the $g_c \ll g_L$ limit.

Spontaneous emission of the DTC, whatever the underlying source of fluctuations, is a source of Purcell decay

for the qubits whose rate can be approximated as, $\Gamma_{1,a} = (g_a/\Delta_a)^2\Gamma_{1,1}$ and $\Gamma_{1,b} = (g_b/\Delta_b)^2\Gamma_{1,2}$ where $\Gamma_{1,j}$ for $j \in \{a, 1, 2, b\}$ is the relaxation rate of the relevant transmon. Multijunction transmon devices routinely have lifetimes in excess of tens of microseconds. Assuming $T_1 > 20 \mu\text{s}$ and a Purcell factor $(g_j/\Delta_j)^2 \sim 1/10$, the coupler transmons impose at worst a 200- μs energy relaxation time on each qubit. While the dispersive regime is considered to be $(g_j/\Delta_j) < 0.1$, violating the dispersive approximation condition requires renormalization of (g_j/Δ_j) and the inclusion of fourth-order terms in the Schrieffer-Wolff transformation for quantitative accuracy [47] and accounts for the deviation between Eqs. (C23) and (C29) and numerical simulations in Figs. 2 and 4, respectively.

The impact of DTC-induced dephasing on the qubits can be computed from the frequency response of its eigenstates in the presence of fluctuations on loop flux of the SQUID. The coupler eigenenergies change by at most $4g_L$ over the full flux tuning range, with a maximum slope at the idling flux typically set to the decoupling bias $\Phi_e^{(0)}$. At the idling flux, the slope is then $|\partial\omega/\partial\Phi| = 2g_L/\varphi_0$. For typical amplitudes of flux noise spectral density, $\sqrt{A_\Phi} \sim 2.5\mu\Phi_0/\sqrt{\text{Hz}}$, the Hahn-echo dephasing rate due to $1/f$ flux noise can be estimated as $\Gamma_\phi^E = \sqrt{A_\Phi} \ln(2)|\partial\omega/\partial\Phi| \sim 50 \times 10^3 \text{ s}^{-1/2}$ [48]. The frequency fluctuations of the qubits due to flux- and critical-current noise of the coupler transmons are filtered by the Purcell factor $(g_j/\Delta_j)^2$. Hence for a Purcell factor of $1/10$, $1/f$ flux noise would limit the coherence of coupled qubit modes to approximately 200 μs at $\Phi_e^{(0)}$.

In summary, we theoretically explore the use of hybridization between two transmons, a DTC, as a mechanism for mediating tunable interactions between fixed-frequency qubits. The DTC design offers low noise, along with linear and easy-to-model qubit-qubit interactions. Crucially, the decoupling condition is defined by a flux bias that nulls the hybridization, making the decoupling condition almost entirely independent of the properties of the data qubit and qubit-DTC interaction. The extra design freedom afforded by having two coupler transmons rather than one also enables implementation of fast, parametric coupling to a fixed mode or continuum. Moreover, the DTC may be attractive as a standalone qubit for its gentle eigenfrequency tuning with flux, weak exchange coupling with its current bias line, and level structure. The last benefit may also enable alternative qutrit-based superconducting circuit architectures [49,50].

ACKNOWLEDGMENTS

This material is based upon work supported by the U.S. Department of Energy, Office of Science, under award number DE-SC0019461, and Air Force Office of Scientific Research (AFOSR) under grant FA9550-21-1-0151. D.L.C. and M.D.L. acknowledge support from AFOSR

grant LRIR#22RICOR003. Any opinions, findings, and conclusions or recommendations expressed in this article are those of the authors and do not necessarily reflect the views of the Air Force Research Laboratory (AFRL). Approved for public release: PA#AFRL-2023-2076.

APPENDIX A: CIRCUIT DERIVATION FOR THE COUPLER ALONE

We write down the Lagrangian for the circuit shown in Fig. 5 using standard circuit parametrization [51–53]

$$\begin{aligned} \mathcal{L} = & \frac{1}{2}C_1(\dot{\Phi}_1 + \dot{\Phi}_{e1})^2 + \frac{1}{2}C_{12}(\dot{\Phi}_2 - \dot{\Phi}_1 + \dot{\Phi}_{e12})^2 \\ & + \frac{1}{2}C_2(\dot{\Phi}_2 - \dot{\Phi}_{e2})^2 + E_1 \cos((\Phi_1 + \Phi_{e1})/\varphi_0) \\ & + E_2 \cos((\Phi_2 - \Phi_{e2})/\varphi_0) \\ & + E_{12} \cos((\Phi_2 - \Phi_1 + \Phi_{e12})/\varphi_0), \end{aligned} \quad (\text{A1})$$

where we use φ_0 to denote the reduced flux quantum $\Phi_0/2\pi$. Here $\Phi_j(t)$ represent the node fluxes (a ‘‘positionlike’’ variable) and $\dot{\Phi}_j(t)$ represent the node voltages (associated ‘‘velocities’’), respectively. The loop of three Josephson junctions is threaded by an external flux, $\Phi_e = \Phi_{e12} + \Phi_{e1} + \Phi_{e2}$, with parameters $\{\Phi_{e12}, \Phi_{e1}, \Phi_{e2}\}$ representing the external flux drops across the three junctions $\{E_{12}, E_1, E_2\}$, respectively.

Performing the Legendre transformation, we arrive at the Hamiltonian,

$$\begin{aligned} H = & \frac{C_{12}(Q_1 + Q_2)^2}{2C^2} + \frac{C_2Q_1^2 + C_1Q_2^2}{2C^2} \\ & + \frac{\dot{\Phi}_{e12}(-Q_1C_2C_{12} + Q_2C_1C_{12})}{C^2} \\ & + \frac{\dot{\Phi}_{e1}(Q_1(C_1C_2 + C_1C_{12}) + Q_2C_1C_{12})}{C^2} \\ & - \frac{\dot{\Phi}_{e2}(Q_1C_1C_{12} + Q_2(C_1C_2 + C_1C_{12}))}{C^2} \\ & - E_1 \cos((\Phi_1 + \Phi_{e1})/\varphi_0) - E_2 \cos((\Phi_2 - \Phi_{e2})/\varphi_0) \\ & - E_{12} \cos((\Phi_2 - \Phi_1 + \Phi_{e12})/\varphi_0), \end{aligned} \quad (\text{A2})$$

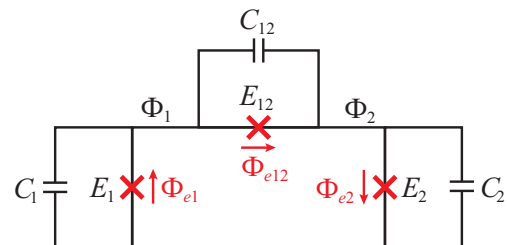


FIG. 5. Coupler circuit comprising two transmons qubits arranged in a flux-tunable loop with a third junction (E_{12}, C_{12}).

TABLE I. Parameter definitions.

Term	Value
C_{S1}	$\frac{C^2}{C_{12} + C_2}$
C_{S2}	$\frac{C^2}{C_{12} + C_1}$
L_j	$\frac{\varphi_0^2}{E'_{12} + E'_j}$
E_{Cj}	$e^2/2C_{Sj}$
g_C	$\frac{C_{12}\sqrt{\omega_1\omega_2}}{2\sqrt{(C_1 + C_{12})(C_2 + C_{12})}}$
g_L	$\frac{4E'_{12}\sqrt{E_{C1}E_{C2}}}{\hbar^2\sqrt{\omega_1\omega_2}}$
ξ_1	$\frac{(2(E'_1 + E'_{12}))^{1/4}[-E'_1(E'_2 + E'_{12})C_2C_{12} + E'_2E'_{12}(C_1C_2 + C_1C_{12})]}{2E_{C2}^{1/4}E'_1E'_2C^2}$
ξ_2	$\frac{(2(E'_2 + E'_{12}))^{1/4}[E'_2(E'_1 + E'_{12})C_1C_{12} - E'_1E'_{12}(C_1C_2 + C_2C_{12})]}{2E_{C2}^{1/4}E'_1E'_2C^2}$
ω_j	$\frac{\sqrt{8(E'_j + E'_{12})E_{Cj}}}{\hbar}$
$v_j^{(4)}$	$\frac{E_{Cj}}{12\hbar}$
$v_j^{(6)}$	$\frac{\sqrt{2}E_{Cj}}{360\hbar} \left(\frac{E_{Cj}}{E'_j + E'_{12}} \right)^{1/2}$
$\mu_k^{(4)}$	$\binom{4}{k} \frac{(-1)^k E'_{12}}{12\hbar} \left(\frac{E_{C1}}{E'_1 + E'_{12}} \right)^{k/4} \left(\frac{E_{C2}}{E'_2 + E'_{12}} \right)^{(4-k)/4}$
$\mu_k^{(6)}$	$\binom{6}{k} \frac{(-1)^k \sqrt{2} E'_{12}}{360\hbar} \left(\frac{E_{C1}}{E'_1 + E'_{12}} \right)^{k/4} \left(\frac{E_{C2}}{E'_2 + E'_{12}} \right)^{(6-k)/4}$

where $C^2 = C_1C_2 + C_1C_{12} + C_2C_{12}$. Using the loop constraint we may parametrize $\{\Phi_{e12}, \Phi_{e1}, \Phi_{e2}\}$ in terms of Φ_e such that all $\dot{\Phi}_e$ terms cancel [53]:

$$\begin{aligned}
H = & \frac{C_{12}(Q_1 + Q_2)^2}{2C^2} + \frac{C_2Q_1^2 + C_1Q_2^2}{2C^2} \\
& - E_1 \cos \left[\left(\Phi_1 + \frac{C_{12}C_2}{C^2} \Phi_e \right) / \varphi_0 \right] \\
& - E_2 \cos \left[\left(\Phi_2 - \frac{C_{12}C_1}{C^2} \Phi_e \right) / \varphi_0 \right] \\
& - E_{12} \cos \left[\left(\Phi_2 - \Phi_1 + \frac{C_1C_2}{C^2} \Phi_e \right) / \varphi_0 \right]. \quad (\text{A3})
\end{aligned}$$

In this parameterization, we can infer that for typical capacitive coupling, $C_{12} \leq 0.1\sqrt{C_1C_2}$, the participation of E_{12} with Φ_e is greater than 80%. Due to the lack of $\dot{\Phi}_e$ terms, Eq. (A3) is the simplest construction for charge-basis simulations of the Hamiltonian.

Another useful parameterization redistributes Φ_e across the junctions to set $\partial H / \partial \Phi_j = 0$ for $j = \{1, 2\}$. This cancels odd order terms in Φ_j and thereby enables a straightforward conversion to the harmonic oscillator basis. We assume $\langle \Phi_j^2 \rangle \ll \Phi_0$ and expand to fourth order in Φ_j

$$\begin{aligned}
H \approx & \frac{C_{12}(Q_1 + Q_2)^2}{2C^2} + \frac{C_2Q_1^2 + C_1Q_2^2}{2C^2} \\
& + \frac{\dot{\Phi}_{e12}(-Q_1C_2C_{12} + Q_2C_1C_{12})}{C^2} \\
& + \frac{E'_{12}\dot{\Phi}_{e12}}{E'_1} \frac{(Q_1(C_1C_2 + C_1C_{12}) + Q_2C_1C_{12})}{C^2} \\
& - \frac{E'_{12}\dot{\Phi}_{e12}}{E'_2} \frac{(Q_1C_2C_{12} + Q_2(C_1C_2 + C_2C_{12}))}{C^2} \\
& + E'_1 \left(\frac{\Phi_1^2}{2\varphi_0^2} - \frac{\Phi_1^4}{24\varphi_0^4} \right) + E'_2 \left(\frac{\Phi_2^2}{2\varphi_0^2} - \frac{\Phi_2^4}{24\varphi_0^4} \right) \\
& + E'_{12} \left(\frac{(\Phi_2 - \Phi_1)^2}{2\varphi_0^2} - \frac{(\Phi_2 - \Phi_1)^4}{24\varphi_0^4} \right). \quad (\text{A4})
\end{aligned}$$

The external flux is then

$$\Phi_e = \Phi_{e12} + \varphi_0 \arcsin((E_{12}/E_1) \sin(\Phi_{e12}/\varphi_0)) + \varphi_0 \arcsin((E_{12}/E_2) \sin(\Phi_{e12}/\varphi_0)), \quad (\text{A5})$$

which may be numerically inverted. The junction energies are now flux sensitive: $E'_{12} = E_{12} \cos(\Phi_{e12}/\varphi_0)$ and $E'_j = \sqrt{E_j^2 - E_{12}^2 \sin^2(\Phi_{e12}/\varphi_0)}$.

1. Harmonic oscillator basis

We convert to the harmonic oscillator basis by substituting $Q_j = \sqrt{\hbar\omega_j C_{Sj}/2}(a_j + a_j^\dagger)$ and $\Phi_j = -i\sqrt{\hbar\omega_j L_j/2}(a_j - a_j^\dagger)$ in Eq. (A4). This leads to the following approximate Hamiltonian, with parameters defined in Table I, as

$$\begin{aligned} H/\hbar = & \sum_{j=1}^2 \left[\omega_j a_j^\dagger a_j - v_j^{(4)} (a_j - a_j^\dagger)^4 - v_j^{(6)} (a_j - a_j^\dagger)^6 \right] \\ & + g_C (a_1 + a_1^\dagger)(a_2 + a_2^\dagger) + g_L (a_1 - a_1^\dagger)(a_2 - a_2^\dagger) \\ & + \sum_{j=1}^2 \frac{\xi_j \dot{\Phi}_{e12}}{\Phi_0} (a_j + a_j^\dagger) \\ & - \sum_{k=1}^3 \mu_k^{(4)} (a_1 - a_1^\dagger)^k (a_2 - a_2^\dagger)^{(4-k)} \\ & - \sum_{k=1}^3 \mu_k^{(6)} (a_1 - a_1^\dagger)^k (a_2 - a_2^\dagger)^{(6-k)}. \end{aligned} \quad (\text{A6})$$

The terms fourth order in the raising and lowering operators modify the eigenenergies in the harmonic oscillator basis by several hundred MHz and account for the majority of the anharmonicity. The sixth-order terms compensate for a residual few 10 s of MHz of discrepancy between the charge basis and harmonic oscillator approaches to simulation. At sixth order in the raising and lowering operators the first- and second-excitation manifolds of eigenenergies for the two simulation approaches agree to within 1 MHz, shown together in Fig. 6.

APPENDIX B: CIRCUIT DERIVATION FOR COUPLER AND DATA QUBITS

We now include the data-qubit terms to the Lagrangian in Eq. (A1), collect the capacitive terms between operators, and break out the time dependence of the flux

$$\begin{aligned} \mathcal{L} = & \frac{1}{2} \vec{\Phi}^T \check{C} \vec{\Phi} + \dot{\Phi}_1 (C_1 \dot{\Phi}_{e1} - C_{12} \dot{\Phi}_{e12}) \\ & - \dot{\Phi}_2 (C_2 \dot{\Phi}_{e2} - C_{12} \dot{\Phi}_{e12}) + E_1 \cos((\Phi_1 + \Phi_{e1})/\varphi_0) \end{aligned}$$

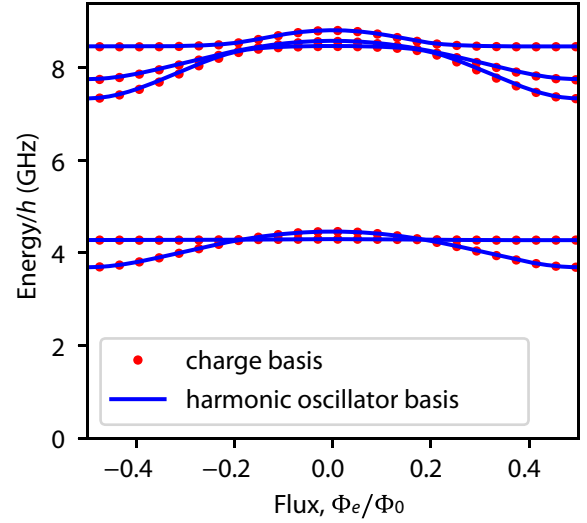


FIG. 6. Comparison of the simulated eigenenergies found by a harmonic oscillator basis simulation [Eq. (A3)] versus a charge-basis simulation [A6]. We choose parameters $E_j = 13$ GHz, $E_{12} = 1.3$ GHz, $C_j = 100$ fF, and $C_{12} = 0$ fF. We simulate eight levels per qubit for the harmonic oscillator simulation and 14 Cooper-pair levels in the charge simulation.

$$\begin{aligned} & + E_2 \cos((\Phi_2 - \Phi_{e2})/\varphi_0) \\ & + E_{12} \cos((\Phi_2 - \Phi_1 + \Phi_{e12})/\varphi_0) \\ & + E_a \cos(\Phi_a/\varphi_0) + E_b \cos(\Phi_b/\varphi_0), \end{aligned} \quad (\text{B1})$$

where $\vec{\Phi} = (\dot{\Phi}_a, \dot{\Phi}_1, \dot{\Phi}_2, \dot{\Phi}_b)^T$ and the capacitance matrix is given by,

$$\begin{pmatrix} C_a & C_{a1} & 0 & 0 \\ C_{a1} & C_1 & C_{12} & 0 \\ 0 & C_{12} & C_2 & C_{b2} \\ 0 & 0 & C_{b2} & C_b \end{pmatrix}. \quad (\text{B2})$$

Performing the Legendre transformation, we arrive at the Hamiltonian,

$$\begin{aligned} \mathcal{H} = & \frac{1}{2} \vec{Q}^T \check{C}^{-1} \vec{Q} + \vec{Q}^T \check{C}^{-1} \begin{pmatrix} 0 \\ C_1 \dot{\Phi}_{e1} - C_{12} \dot{\Phi}_{e12} \\ -C_2 \dot{\Phi}_{e2} + C_{12} \dot{\Phi}_{e12} \\ 0 \end{pmatrix} \\ & + E_1 \cos((\Phi_1 + \Phi_{e1})/\varphi_0) \\ & + E_2 \cos((\Phi_2 - \Phi_{e2})/\varphi_0) \\ & + E_{12} \cos((\Phi_2 - \Phi_1 + \Phi_{e12})/\varphi_0) \\ & + E_a \cos(\Phi_a/\varphi_0) + E_b \cos(\Phi_b/\varphi_0), \end{aligned} \quad (\text{B3})$$

where $\vec{Q}^T = (Q_a, Q_1, Q_2, Q_b)$ and Q_j for $j \in \{a, 1, 2, b\}$ are charge operators for the j 'th transmon. If C_{1a} , C_{2b} , and C_{12} are all nonzero, then direct capacitive coupling exists between all qubits.

Using the loop constraint we may parametrize $\{\Phi_{e12}, \Phi_{e1}, \Phi_{e2}\}$ such that all $\dot{\Phi}_e$ terms cancel [53]:

$$H = \frac{1}{2} \vec{Q}^T \check{C}^{-1} \vec{Q} - E_1 \cos \left[\left(\Phi_1 + \frac{C_{12} C_2}{C^2} \Phi_e \right) / \varphi_0 \right] - E_2 \cos \left[\left(\Phi_2 - \frac{C_{12} C_1}{C^2} \Phi_e \right) / \varphi_0 \right] - E_{12} \cos \left[\left(\Phi_2 - \Phi_1 + \frac{C_1 C_2}{C^2} \Phi_e \right) / \varphi_0 \right]. \quad (\text{B4})$$

Interestingly, this parameterization of the flux does not change from that of the coupler alone in Eq. (A3). Due to the lack of $\dot{\Phi}_e$ terms, Eq. (B4) is the simplest construction for charge-basis simulations of the full qubit and coupler Hamiltonian.

1. Approximations for harmonic oscillator basis

Another useful parameterization involves expanding the cosine terms in the Hamiltonian according to

$$\cos(\Phi + \Phi_e) \approx \cos(\Phi) \cos(\Phi_e) + \sin(\Phi) \sin(\Phi_e), \quad (\text{B5})$$

$$\approx \cos(\Phi) \cos(\Phi_e) + \Phi \sin(\Phi_e), \quad (\text{B6})$$

where we assume $\langle \Phi_j^2 \rangle \ll \Phi_0$, which is appropriate in the transmon limit $E_J/E_C > 50$.

If, after expanding in Φ_j and $\dot{\Phi}_j$, the largest terms are proportional to Φ_j^2 and $\dot{\Phi}_j^2$ the harmonic oscillator basis can require fewer states to be modeled relative to the charge basis while achieving equivalent numerical precision. In flux-sensitive systems this can require some extra work since the external flux must be distributed across the junctions so that terms linear in Φ_j cancel. Solving the following equations, separately for Φ_{e1} and Φ_{e2} , performs this cancellation:

$$E_1 \sin(\Phi_{e1}) = E_{12} \sin(\Phi_{e12}), \quad (\text{B7})$$

$$E_2 \sin(\Phi_{e2}) = E_{12} \sin(\Phi_{e12}),$$

$$\Phi_{e1} = \arcsin(E_{12} \sin(\Phi_{e12})/E_1), \quad (\text{B8})$$

$$\Phi_{e2} = \arcsin(E_{12} \sin(\Phi_{e12})/E_2),$$

$$\dot{\Phi}_{e1} = E'_{12} \dot{\Phi}_{e12}/E'_1, \quad (\text{B9})$$

$$\dot{\Phi}_{e2} = E'_{12} \dot{\Phi}_{e12}/E'_2,$$

$$E'_{12} = E_{12} \cos(\Phi_{e12}/\varphi_0), \quad (\text{B10})$$

$$E'_1 = \sqrt{E_1^2 - E_{12}^2 \sin^2(\Phi_{e12}/\varphi_0)}, \quad (\text{B11})$$

$$E'_2 = \sqrt{E_2^2 - E_{12}^2 \sin^2(\Phi_{e12}/\varphi_0)}. \quad (\text{B12})$$

Substituting into Eq. (B3) and truncating at sixth order in Φ_j we arrive at a suitable starting point for a transformation to the harmonic oscillator basis:

$$H \approx \frac{1}{2} \vec{Q}^T \check{C}^{-1} \vec{Q} + \vec{Q}^T \check{C}^{-1} \begin{pmatrix} 0 \\ (C_1 E'_{12}/E'_1 - C_{12}) \dot{\Phi}_{e12} \\ (-C_2 E'_{12}/E'_2 + C_{12}) \dot{\Phi}_{e12} \\ 0 \end{pmatrix} + E'_1 \left(\frac{\Phi_1^2}{2\varphi_0^2} - \frac{\Phi_1^4}{24\varphi_0^4} + \frac{\Phi_1^6}{720\varphi_0^6} \right) + E'_2 \left(\frac{\Phi_2^2}{2\varphi_0^2} - \frac{\Phi_2^4}{24\varphi_0^4} + \frac{\Phi_2^6}{720\varphi_0^6} \right) + E'_{12} \left(\frac{(\Phi_2 - \Phi_1)^2}{2\varphi_0^2} - \frac{(\Phi_2 - \Phi_1)^4}{24\varphi_0^4} + \frac{(\Phi_2 - \Phi_1)^6}{720\varphi_0^6} \right). \quad (\text{B13})$$

E'_1 , E'_2 , and E'_{12} are parametrized by Φ_{e12} . Φ_{e12} is related to the true externally applied flux Φ_e by the following relation:

$$\Phi_e = \Phi_{e12} + \varphi_0 \arcsin((E_{12}/E_1) \sin(\Phi_{e12}/\varphi_0)) + \varphi_0 \arcsin((E_{12}/E_2) \sin(\Phi_{e12}/\varphi_0)), \quad (\text{B14})$$

which may be numerically inverted.

2. Hamiltonian for the full circuit in the harmonic oscillator basis

We convert to the harmonic oscillator basis by substituting $Q_j = \sqrt{\hbar\omega_j} C_{Sj}/2(a_j + a_j^\dagger)$ and $\Phi_j = -i\sqrt{\hbar\omega_j} L_j/2(a_j - a_j^\dagger)$ in Eq. (B13) for $j \in \{a, 1, 2, b\}$.

This leads to the following approximate Hamiltonian given in Eq. (B15), with parameters defined in Table II.

$$H/\hbar = \sum_j \left[\omega_j a_j^\dagger a_j - v_j^{(4)} (a_j - a_j^\dagger)^4 - v_j^{(6)} (a_j - a_j^\dagger)^6 \right] + \sum_{j \neq k} g_{Cj,k} (a_j + a_j^\dagger)(a_k + a_k^\dagger) + g_L (a_1 - a_1^\dagger)(a_2 - a_2^\dagger) + \sum_j \frac{\xi_j \dot{\Phi}_{e12}}{\Phi_0} (a_j + a_j^\dagger) - \sum_{\ell=1}^3 \mu_\ell^{(4)} (a_1 - a_1^\dagger)^\ell (a_2 - a_2^\dagger)^{(4-\ell)} - \sum_{\ell=1}^3 \mu_\ell^{(6)} (a_1 - a_1^\dagger)^\ell (a_2 - a_2^\dagger)^{(6-\ell)} \quad (\text{B15})$$

where the summations range over $j, k \in \{a, 1, 2, b\}$.

TABLE II. Parameter definitions.

Term	Value
$C_{Sj,j}$	$1/C_{j,j}^{-1}$
L_j for $j \in \{1, 2\}$	$\varphi_0^2/(E'_{12} + E'_j)$
L_j for $j \in \{a, b\}$	φ_0^2/E_j
Z_j	$\sqrt{L_j/C_{Sj,j}}$
E_{Cj}	$e^2/2C_{Sj,j}$
$g_{Cj,k}$	$C_{j,k}^{-1}/2\sqrt{Z_j Z_k}$
g_L	$E'_{12}\sqrt{Z_j Z_k}/2\varphi_0^2$
ξ_j	$\Phi_0[C_{j,1}^{-1}(C_1 E'_{12}/E'_1 - C_{12})$ $+ C_{j,2}^{-1}(-C_2 E'_{12}/E'_2 + C_{12})]/\sqrt{2\hbar Z_j}$
$\hbar\omega_j$	$\sqrt{8(E'_j + E'_{12})E_{Cj}}$
$v_j^{(4)}$	$\frac{E_{Cj}}{12\hbar}$
$v_j^{(6)}$	$\frac{\sqrt{2}E_{Cj}}{360\hbar} \left(\frac{E_{Cj}}{E'_j + E'_{12}}\right)^{1/2}$
$\mu_k^{(4)}$	$\binom{4}{k} \frac{(-1)^k E'_{12}}{12\hbar} \left(\frac{E_{C1}}{E'_1 + E'_{12}}\right)^{k/4}$ $\times \left(\frac{E_{C2}}{E'_2 + E'_{12}}\right)^{(4-k)/4}$
$\mu_k^{(6)}$	$\binom{6}{k} \frac{(-1)^k \sqrt{2}E'_{12}}{360\hbar} \left(\frac{E_{C1}}{E'_1 + E'_{12}}\right)^{k/4}$ $\times \left(\frac{E_{C2}}{E'_2 + E'_{12}}\right)^{(6-k)/4}$

The inverted capacitance matrix results in effective capacitive coupling between all four transmons in the system. We represent the exact analytic form followed by three approximate examples:

$$g_{j,k} = \frac{|A_{s\setminus j, s\setminus k}| \sqrt{\omega_j \omega_k}}{2\sqrt{|A_{s\setminus j, s\setminus j}| |A_{s\setminus k, s\setminus k}|}}, \quad (\text{B16})$$

$$g_{a,1} \approx C_{a1} \sqrt{\omega_a \omega_1} / C_S, \quad (\text{B17})$$

$$g_{a,2} \approx C_{a1} C_{12} \sqrt{\omega_a \omega_2} / C_S^2, \quad (\text{B18})$$

$$g_{a,b} \approx C_{a1} C_{b2} C_{12} \sqrt{\omega_a \omega_b} / C_S^3, \quad (\text{B19})$$

where $s = \{a, 1, 2, b\}$, A is the capacitance matrix from the Lagrangian, $|A|$ is the determinant of that matrix, and $A_{s\setminus j, s\setminus k}$ is the four-transmon capacitance matrix with row j and column k deleted. In Eqs. (B17)–(B19), C_S is a stand in for something with the approximate value of the shunt capacitance, such as C_{Sj} . The approximate relations $g_{a,1}$, $g_{a,2}$, and $g_{a,b}$ show that the coupling capacitance falls off geometrically as the coupling progresses from nearest neighbor to next-to-nearest neighbor and then to next-to-next-to-nearest neighbor coupling, respectively. Data

TABLE III. Commonly used shorthand notation in the appendices.

Term	Shorthand
$g_{C1,2}$	g_C
$g_{Ca,1}$	g_a
$g_{C2,b}$	g_b

transmons a and b are, therefore, well isolated from each other, capacitively, by the coupler circuit.

For notational simplicity we use the shorthand in Table III in the following appendices.

3. Simulation of parametric driving

We simulate the parametric driving that appears in Fig. 4 with Eq. (B15). Every term in Eq. (B15) is flux sensitive. Those parameters, defined in Table II, are flux sensitive through the definitions of E'_{12} and E'_j [Eqs. (B10)–(B12)] and Φ_{e12} [Eq. (B14)]. We apply a 50-ns half cosine ramp to a flux drive amplitude $A\Phi_0$. The drive $\Phi_e(t) = (A \sin(\omega_d t) - 0.25)\Phi_0$ is then held constant for 160 ns. The qubit state's time evolution is modeled using the qutip python package's time-dependent mesolve ODE solver in the absence of dissipation [54,55]. Realistic estimates for energy relaxation and decoherence for the proposed tunable coupler are provided in Sec. D.

APPENDIX C: ANALYTICAL DERIVATION OF THE EFFECTIVE COUPLING

To apply the standard machinery of the Schrieffer-Wolff transformation to decouple the states of the coupler from the computational Hilbert space we must first diagonalize the coupler states. Exact analytic diagonalization at second order in raising and lowering operators (this neglects anharmonicity, which first appears at fourth order in the raising and lowering operators) may be performed using the Bogoliubov transformation $\Psi = T\Psi'$ where $\Psi^\dagger = (a_1 \ a_1^\dagger \ a_2 \ a_2^\dagger)$ is the untransformed “vector” of raising and lowering operators. Our goal is to analytically obtain “ T .” To this end, we define $\Psi^\dagger K \Psi$ where K contains prefactors associated with the quadratic terms of the coupler Hamiltonian [Eq. (A6)]

$$K = \begin{pmatrix} \omega_1 & 0 & g_C - g_L & g_C + g_L \\ 0 & \omega_1 & g_C + g_L & g_C - g_L \\ g_C - g_L & g_C + g_L & \omega_2 & 0 \\ g_C + g_L & g_C - g_L & 0 & \omega_2 \end{pmatrix}. \quad (\text{C1})$$

Note that we use the shorthand notation introduced in Table III. The idea is to perform a similarity transformation T to diagonalize K and thereby find the desired Bogoliubov transformation.

Interestingly, because $[\Psi_i^\dagger, \Psi_j] = (-1)^i \delta_{ij}$, a similarity transformation is likely to produce a set of transformed

operators that no longer obey the bosonic commutation relations. We can fix this by identifying the transformation $\sigma = (-1)^i \delta_{ij}$, and applying it to the column vector $[\Psi_i^\dagger, \sigma \Psi_j] = \sigma \sigma = \delta_{ij}$, where the commutation relations are now uniform. A similarity transformation T may be constructed

$$\sigma T^\dagger \sigma \sigma K T = T^{-1} \sigma K T = \sigma K', \quad (\text{C2})$$

where K' is the desired diagonal form of K and $\Psi = T\Psi'$, see Altland and Simons, p. 72 [56]. Using this technique, the diagonal form of the coupler operators, given by Ψ' , can be found by diagonalizing σK to obtain the transformation T .

The diagonal elements of K' are a redundant set of eigenenergies $\{\omega_\pm, -\omega_\pm\}$ otherwise obtainable from the Hamiltonian of the system (again this assumes a perfectly linear system). Starting from Eq. (C1) these are,

$$\omega_\pm = \sqrt{2\bar{\omega}^2 - \omega_1\omega_2 - 4g_{C12}g_L \pm 2\eta}, \quad (\text{C3})$$

with $\eta = \sqrt{\delta^2\bar{\omega}^2 + (g_C + g_L)^2\omega_1\omega_2 - 4g_Cg_L\bar{\omega}^2}$. An analytic form for the eigenstates is also required to obtain an effective coupling but there exists no short-form expression for these. Inspection of Eq. (C1) reveals that the terms proportional to $g_C + g_L$, the counter-rotating terms, and the terms proportional to $g_C - g_L$, the co-rotating terms, interact with each other at second order in $(g_C \pm g_L)/\omega_j$. This weak interaction between co- and counter-rotating terms justifies separating the calculation of g_{eff} into two parts, greatly simplifying the analytic expression of the eigenstates. The contributions to g_{eff} are then added together to obtain a better approximation of the effective coupling.

1. Co-rotating terms

Neglecting terms proportional to $g_C + g_L$ in Eq. (C1) allows a compact representation of the approximate eigenvectors T , which we apply to derive an analytic form of the effective coupling as mediated by exchange interactions. The approximate eigenenergies are likewise simplified to

$$\omega_\pm = \bar{\omega} \pm \sqrt{\delta^2 + (g_C - g_L)^2}, \quad (\text{C4})$$

where $\bar{\omega} = (\omega_1 + \omega_2)/2$ and $\delta = (\omega_1 - \omega_2)/2$. The corresponding eigenvectors now take the form

$$a_- = -\sqrt{1 - \beta^2}a_1 + \beta a_2, \quad (\text{C5a})$$

$$a_+ = \beta a_1 + \sqrt{1 - \beta^2}a_2, \quad (\text{C5b})$$

where $\beta = A/\sqrt{(g_C - g_L)^2 + A^2}$, with $A = \delta + \sqrt{\delta^2 + (g_C - g_L)^2}$. If $\delta = 0$ then the coupler transmons are degenerate and therefore fully hybridized, leading to

$\beta = 1/\sqrt{2}$ as we might expect. Substituting the eigenoperators a_\pm for $a_{1,2}$ in Eq. (A6) and retaining terms to second order, we obtain

$$H = H_0 + V, \quad (\text{C6})$$

with

$$H_0/\hbar = \omega_a a_a^\dagger a_a + \omega_b a_b^\dagger a_b + \omega_- a_-^\dagger a_- + \omega_+ a_+^\dagger a_+, \quad (\text{C7a})$$

$$\begin{aligned} V/\hbar = & (-\sqrt{1 - \beta^2}g_a + \beta g_{Ca,2})(a_a + a_a^\dagger)(a_- + a_-^\dagger) \\ & + (\beta g_b - \sqrt{1 - \beta^2}g_{Cb,1})(a_b + a_b^\dagger)(a_- + a_-^\dagger) \\ & + (\beta g_a + \sqrt{1 - \beta^2}g_{Ca,2})(a_a + a_a^\dagger)(a_+ + a_+^\dagger) \\ & + (\sqrt{1 - \beta^2}g_b + \beta g_{Cb,1})(a_b + a_b^\dagger)(a_+ + a_+^\dagger). \end{aligned} \quad (\text{C7b})$$

We identify a Schrieffer-Wolff generator S such that $[H_0, S] = V$,

$$\begin{aligned} S/\hbar = & \frac{-\sqrt{1 - \beta^2}g_a + \beta g_{Ca,2}}{\Delta_{a-}}(a_a^\dagger a_- - a_a a_-^\dagger) \\ & + \frac{\beta g_b - \sqrt{1 - \beta^2}g_{Cb,1}}{\Delta_{b-}}(a_b^\dagger a_- - a_b a_-^\dagger) \\ & + \frac{\beta g_a + \sqrt{1 - \beta^2}g_{Ca,2}}{\Delta_{a+}}(a_a^\dagger a_+ - a_a a_+^\dagger) \\ & + \frac{\sqrt{1 - \beta^2}g_b + \beta g_{Cb,1}}{\Delta_{b+}}(a_b^\dagger a_+ - a_b a_+^\dagger) \\ & + \frac{-\sqrt{1 - \beta^2}g_a + \beta g_{Ca,2}}{\Sigma_{a-}}(a_a^\dagger a_-^\dagger - a_a a_-) \\ & + \frac{\beta g_b - \sqrt{1 - \beta^2}g_{Cb,1}}{\Sigma_{b-}}(a_b^\dagger a_-^\dagger - a_b a_-) \\ & + \frac{\beta g_a + \sqrt{1 - \beta^2}g_{Ca,2}}{\Sigma_{a+}}(a_a^\dagger a_+^\dagger - a_a a_+) \\ & + \frac{\sqrt{1 - \beta^2}g_b + \beta g_{Cb,1}}{\Sigma_{b+}}(a_b^\dagger a_+^\dagger - a_b a_+), \end{aligned} \quad (\text{C8})$$

where $\Delta_{j\pm} = \omega_j - \omega_\pm = \Delta_j \pm \sqrt{\delta^2 + (g_C - g_L)^2}$, $\Sigma_{j\pm} = \omega_j + \omega_\pm = \Sigma_j \pm \sqrt{\delta^2 + (g_C - g_L)^2}$, $\Sigma_j = \omega_j + \bar{\omega}$, and as defined in the main text $\Delta_j = \omega_j - \bar{\omega}$. Then

$$H' = e^S H e^{-S} = H_0 + [S, V]/2 + \mathcal{O}(V^3) \quad (\text{C9})$$

is the leading-order diagonalized Hamiltonian with the prefactor of the lowest order term $[S, V]/2$ setting the

effective coupling

$$\begin{aligned}
 g_{\text{eff}}^{\text{co}} &= \frac{(g_a g_b + g_{Ca,2} g_{Cb,1}) \beta \sqrt{1 - \beta^2}}{2} \\
 &\times \sum_{j=a,b} \left[\frac{1}{\Delta_{j+}} - \frac{1}{\Delta_{j-}} + \frac{1}{\Sigma_{j+}} - \frac{1}{\Sigma_{j-}} \right] + \frac{g_{Ca,2} g_b}{2} \\
 &\times \sum_{j=a,b} \left[\frac{1 - \beta^2}{\Delta_{j+}} + \frac{\beta^2}{\Delta_{j-}} + \frac{1 - \beta^2}{\Sigma_{j+}} + \frac{\beta^2}{\Sigma_{j-}} \right] \\
 &+ \frac{g_{Cb,1} g_a}{2} \sum_{j=a,b} \left[\frac{\beta^2}{\Delta_{j+}} + \frac{1 - \beta^2}{\Delta_{j-}} + \frac{\beta^2}{\Sigma_{j+}} + \frac{1 - \beta^2}{\Sigma_{j-}} \right].
 \end{aligned} \tag{C10}$$

We may further condense terms

$$\begin{aligned}
 g_{\text{eff}}^{\text{co}} &= (g_a g_b + g_{Ca,2} g_{Cb,1}) (g_C - g_L) \sum_{j=a,b} \left[\frac{1}{2D_j^2} + \frac{1}{2S_j^2} \right] \\
 &+ g_{Ca,2} g_b \sum_{j=a,b} \left[\frac{\omega_j - \omega_2}{2D_j^2} + \frac{\omega_j - \omega_2}{2S_j^2} \right] \\
 &+ g_{Cb,1} g_a \sum_{j=a,b} \left[\frac{\omega_j - \omega_1}{2D_j^2} + \frac{\omega_j - \omega_1}{2S_j^2} \right],
 \end{aligned} \tag{C11}$$

$$D_j^2 = \Delta_j^2 - \delta^2 - (g_C - g_L)^2, \tag{C12}$$

$$S_j^2 = \Sigma_j^2 - \delta^2 - (g_C - g_L)^2. \tag{C13}$$

The terms proportional to S_j^{-2} and $g_{Ca,2} g_{Cb,1}$ are typically small and may be neglected.

The ac Stark shifts on the data qubits may be calculated similarly. Here we neglect the terms proportional to $g_{Ca,2}$ and $g_{Cb,1}$

$$\begin{aligned}
 \omega_a^{\text{ac}} &= \frac{g_a^2}{2} \left[\frac{\beta^2}{\Delta_{a+}} + \frac{1 - \beta^2}{\Delta_{a-}} - \frac{\beta^2}{\Sigma_{a+}} - \frac{1 - \beta^2}{\Sigma_{a-}} \right], \\
 \omega_a^{\text{ac}} &= \frac{g_a^2}{2} \left[\frac{\omega_a - \omega_1}{D_a^2} + \frac{-\omega_a - \omega_1}{S_a^2} \right], \\
 \omega_b^{\text{ac}} &= \frac{g_b^2}{2} \left[\frac{1 - \beta^2}{\Delta_{b+}} + \frac{\beta^2}{\Delta_{b-}} - \frac{1 - \beta^2}{\Sigma_{b+}} - \frac{\beta^2}{\Sigma_{b-}} \right], \\
 \omega_b^{\text{ac}} &= \frac{g_b^2}{2} \left[\frac{\omega_b - \omega_2}{D_b^2} + \frac{-\omega_b - \omega_2}{S_b^2} \right].
 \end{aligned} \tag{C14}$$

2. Counter-rotating terms

Neglecting now the terms proportional to $g_C - g_L$ in Eq. (C1), the direct exchange interaction terms, we can calculate the approximate eigenenergies,

$$\omega_{\pm} = \pm \delta + \sqrt{\bar{\omega}^2 - (g_C + g_L)^2}, \tag{C15}$$

and the eigenvectors,

$$a_+ = \sqrt{1 + \alpha^2} a_1 - \alpha a_2^\dagger, \tag{C16a}$$

$$a_- = \sqrt{1 + \alpha^2} a_2 - \alpha a_1^\dagger, \tag{C16b}$$

with $\alpha = (g_C + g_L) / \sqrt{-(g_C + g_L)^2 + D^2}$, $D = \bar{\omega} + \sqrt{\bar{\omega}^2 - (g_C + g_L)^2}$. The coefficients of Eqs. (C16a) and (C16b) satisfy the bosonic commutation relations $[a_{\pm}, a_{\pm}^\dagger] = 1$ and $[a_+, a_-] = 0$. Substituting the transformed operators for $a_{1,2}$ in Eq. (A6) leads to the interaction,

$$\begin{aligned}
 V/\hbar &= \alpha g_a (a_a + a_a^\dagger) (a_- + a_-^\dagger) \\
 &+ \sqrt{1 + \alpha^2} g_b (a_b + a_b^\dagger) (a_- + a_-^\dagger) \\
 &+ \sqrt{1 + \alpha^2} g_a (a_a + a_a^\dagger) (a_+ + a_+^\dagger) \\
 &+ \alpha g_b (a_b + a_b^\dagger) (a_+ + a_+^\dagger),
 \end{aligned} \tag{C17}$$

which can be transformed using the generator,

$$\begin{aligned}
 S/\hbar &= \frac{\alpha g_a}{\Delta_{a-}} (a_a^\dagger a_- - a_a a_-^\dagger) + \frac{\sqrt{1 + \alpha^2} g_b}{\Delta_{b-}} (a_b^\dagger a_- - a_b a_-^\dagger) \\
 &+ \frac{\sqrt{1 + \alpha^2} g_a}{\Delta_{a+}} (a_a^\dagger a_+ - a_a a_+^\dagger) + \frac{\alpha g_b}{\Delta_{b+}} (a_b^\dagger a_+ - a_b a_+^\dagger) \\
 &+ \frac{\alpha g_a}{\Sigma_{a-}} (a_a^\dagger a_-^\dagger - a_a a_-) + \frac{\sqrt{1 + \alpha^2} g_b}{\Sigma_{b-}} (a_b^\dagger a_-^\dagger - a_b a_-) \\
 &+ \frac{\sqrt{1 + \alpha^2} g_a}{\Sigma_{a+}} (a_a^\dagger a_+^\dagger - a_a a_+) \\
 &+ \frac{\alpha g_b}{\Sigma_{b+}} (a_b^\dagger a_+^\dagger - a_b a_+),
 \end{aligned} \tag{C18}$$

to obtain the effective qubit-qubit coupling,

$$\begin{aligned}
 g_{\text{eff}}^{\text{counter}} &= \frac{\alpha \sqrt{1 + \alpha^2} g_a g_b}{2} \\
 &\times \sum_{j=a,b} \left[\frac{1}{\Delta_{j-}} + \frac{1}{\Delta_{j+}} - \frac{1}{\Sigma_{j-}} - \frac{1}{\Sigma_{j+}} \right].
 \end{aligned} \tag{C19}$$

Approximating $\alpha \sqrt{1 + \alpha^2} \approx (g_C + g_L) / 2\bar{\omega}$ we may further condense the terms in Eq. (C19)

$$g_{\text{eff}}^{\text{counter}} = -g_a g_b (g_C + g_L) \sum_{j=a,b} \left[\frac{\Delta_j / \bar{\omega}}{2D_j^2} - \frac{\Sigma_j / \bar{\omega}}{2S_j^2} \right]. \tag{C20}$$

3. Effective coupling used in the main text

We approximate the effective coupling for four coupled harmonic oscillators (remember that all the previous analysis in this section neglects nonlinearity) as the sum of the

coupling contributions from the co- and counter-rotating terms $g_{\text{eff}}^{\text{HO}} = g_{\text{eff}}^{\text{co}} + g_{\text{eff}}^{\text{counter}}$,

$$g_{\text{eff}}^{\text{HO}} = \sum_{j=a,b} \left[\frac{g_a g_b \left[g_C - g_L - (g_C + g_L) \frac{\Delta_j}{\bar{\omega}} \right]}{2D_j} + g_{Ca,2} g_b \sum_{j=a,b} \frac{\omega_j - \omega_2}{2D_j^2} + g_{Cb,1} g_a \sum_{j=a,b} \frac{\omega_j - \omega_1}{2D_j^2} \right]. \quad (\text{C21})$$

We find $g_{\text{eff}}^{\text{HO}}$ approximates the numerically determined coupling to several percent accuracy when $v_j^{(4)}, v_j^{(6)}, \mu_k^{(4)}, \mu_k^{(6)} = 0$

Our estimate of g_{eff} when $v_j^{(4)}, v_j^{(6)}, \mu_k^{(4)}, \mu_k^{(6)} \neq 0$ can be improved by incorporating the contribution of fourth-order terms in the raising and lowering operators of H in Eq. (B15) at second order in the raising and lowering operators. We then rescale terms previously defined in $g_{\text{eff}}^{\text{HO}}$.

$$\omega'_{a,b} = \omega_{a,b} - 12v_{a,b}, \quad (\text{C22a})$$

$$\omega'_{1,2} = \omega_{1,2} - 2\mu_2^{(4)} - 12v_{1,2}, \quad (\text{C22b})$$

$$\bar{\omega}' = (\omega'_1 + \omega'_2)/2, \quad (\text{C22c})$$

$$\bar{\delta}' = (\omega'_1 - \omega'_2)/2, \quad (\text{C22d})$$

$$\Delta'_j = \omega'_j - \bar{\omega}', \quad (\text{C22e})$$

$$g'_L = g_L - 3(\mu_1^{(4)} + \mu_3^{(4)}), \quad (\text{C22f})$$

$$D_j^{2'} = \Delta_j^{2'} + \delta^{2'} + (g_C - g'_L)^2. \quad (\text{C22g})$$

With these substitutions, we obtain the definition of the effective coupling used in Fig. 2 of the main text.

$$g_{\text{eff}} = \sum_{j=a,b} \frac{g_a g_b \left[g_C - g'_L - (g_C + g'_L) \frac{\Delta'_j}{\bar{\omega}'} \right]}{2D_j'} + g_{Ca,2} g_b \sum_{j=a,b} \frac{\omega'_j - \omega'_2}{2D_j'^2} + g_{Cb,1} g_a \sum_{j=a,b} \frac{\omega'_j - \omega'_1}{2D_j'^2}. \quad (\text{C23})$$

4. Effective parametric coupling used in the main text

For the purposes of calculating g_{eff}^p , we evaluate all the parameters of Table II at $\Phi_{e12} = -0.25\Phi_0$ except g_C and $E'_{12} = E_{12} \cos(\Phi_{e12}/\varphi_0)$ in g_L . We substitute $\Phi_{e12} = A \sin(\omega_d t) \Phi_0 - 0.25\Phi_0$ into the latter term. $\Phi_e \approx \Phi_{e12}$ is an approximation of Eq. (B14) that is valid in the regime $E_{12} \ll E_j$. The drive flux offset $-0.25\Phi_0$ effectively transforms the cosine into a sine, which we expand about

small “ A ”

$$\begin{aligned} \sin(A\Phi_0 \sin(\omega_d t)/\varphi_0) &\approx 2\pi A \sin(\omega_d t) \\ &\quad - (2\pi A)^3 \sin^3(\omega_d t)/6, \quad (\text{C24}) \\ &\approx (2\pi A - (2\pi A)^3/8) \sin(\omega_d t), \quad (\text{C25}) \end{aligned}$$

$$\sin^3(\omega_d t) = \frac{3}{4} \sin(\omega_d t) - \frac{1}{4} \sin(3\omega_d t). \quad (\text{C26})$$

Substituting into g_L we obtain for g_L^p

$$g_L \approx E_{12}(2\pi A - (2\pi A)^3/8) \sin(\omega_d t) \sqrt{Z_1 Z_2}/2\varphi_0^2, \quad (\text{C27})$$

$$g_L^p \approx (2\pi A - (2\pi A)^3/8) g_L(0\Phi_0)/2. \quad (\text{C28})$$

The terms proportional to $\sin(\omega_d t)$ are large when they include g_L and $\mu_k^{(4)}$ in the numerator of Eq. (C23). By contrast, g_C changes very little as a function of flux and may be set to zero. Most other parameters in Table II can be approximately modeled as their static value at $\Phi_{e12} = -0.25\Phi_0$. In the denominator we retain terms without time dependence. This motivates the substitution $(g_C - g_L)^2 \rightarrow (g_L^p)^2/2 + g_C^2$.

$$g_{\text{eff}}^p \approx \sum_{j=a,b} \frac{-g_a g_b g_L^p (1 - \Delta_j^p/\bar{\omega}^p)}{4(D_j^p)^2}. \quad (\text{C29})$$

$$(D_j^p)^2 = (\Delta_j^p)^2 - (\delta^p)^2 - (g_L^p)^2/2 - g_C^2. \quad (\text{C30})$$

APPENDIX D: NOISE ANALYSIS

1. Coherence

The Gaussian pure-dephasing rate due to $1/f$ flux noise is $\Gamma_\phi^E = \sqrt{A_\Phi} \ln 2 |\partial\omega/\partial\Phi|$ for Hahn-echo measurements. It depends upon the noise amplitude $\sqrt{A_\Phi}$, defined at $\omega/2\pi = 1$ Hz, of the power spectral density $S(\omega)_\Phi = A_\Phi/|\omega|$ and the slope of the energy dispersion with flux $\hbar\partial\omega/\partial\Phi$. Careful engineering gives a noise amplitude $\sqrt{A_\Phi} \sim 2.5\mu\Phi_0$.

On the coupler, the peak-to-peak difference in the frequency dispersion is approximately 0.6 GHz, giving $\Gamma_\phi^E \approx 2.5\mu\Phi_0 \sqrt{\ln 2} (2\pi)^2 \times 0.3 \text{ GHz}/\Phi_0 = 1/40 \mu\text{s}$. The noise on g_{eff} from the flux sensitivity on g_L is then reduced by a factor $g_a g_b / (2\Delta_j^2 - 2\delta^2)$. Similarly, frequency noise on the qubits from the flux sensitivity on $\bar{\omega}$ is reduced by a factor of approximately $g_a^2 / (2\Delta_j^2 - 2\delta^2)$. For $g_{\text{eff}} = 2\pi \times 60 \text{ MHz}$, the coupler limits the pure-dephasing lifetime to $T_\phi^E \sim 400 \mu\text{s}$.

2. Energy relaxation

Energy relaxation of a qubit into its nearest-neighbor coupler transmon is approximately given by the Purcell

formula. Using the definitions in the main text and supplement the coupler induces relaxation of qubit a

$$\begin{aligned}\Gamma_{1,a}^{\text{Purcell}} &\approx g_a^2 \left(\frac{\Gamma_{1,+}\beta^2}{\Delta_{a+}^2} + \frac{\Gamma_{1,-}(1-\beta^2)}{\Delta_{a-}^2} \right) \\ &\sim \frac{\Gamma_{1,1}g_a^2}{(\omega_a - \omega_1)^2}.\end{aligned}\quad (\text{D1})$$

Similarly, for qubit b

$$\begin{aligned}\Gamma_{1,b}^{\text{Purcell}} &\approx g_b^2 \left(\frac{\Gamma_{1,-}\beta^2}{\Delta_{b-}^2} + \frac{\Gamma_{1,+}(1-\beta^2)}{\Delta_{b+}^2} \right) \\ &\sim \frac{\Gamma_{1,2}g_b^2}{(\omega_b - \omega_2)^2}.\end{aligned}\quad (\text{D2})$$

The energy relaxation rates for coupler transmons 1 and 2 are given by $\Gamma_{1,1}$ and $\Gamma_{1,2}$, respectively. While these quantities are not true observables of the system since the coupler transmons can be strongly hybridized, we want to emphasize that qubit a is not very sensitive to relaxation channels local to coupler transmon 2, nor is qubit b sensitive to relaxation channels local to coupler transmon 1. In the case of direct measurement of coupler relaxation rates, or if we expect correlated relaxation processes, then $\Gamma_{1,+}$ and $\Gamma_{1,-}$ describe the energy relaxation rate of the upper and lower hybridized states, respectively.

Plugging in 20 μs as a reasonable lower bound on each coupler transmon's energy relaxation lifetime, the induced T_1 on a neighboring data qubit is 220 μs for a g/Δ ratio of 0.3.

3. Coupling a qubit to an open quantum system

We consider coupling qubit “ a ” to a bath as mediated by the tunable coupler. In this scenario a deliberate interaction with the bath induces coupler transmon 2 to relax with rate $\Gamma_{1,2}$ into the bath.

$$\begin{aligned}\Gamma_{1,a} &\approx \Gamma_{1,2}g_a^2\beta^2(1-\beta^2) \left(\frac{1}{\Delta_{a+}^2} + \frac{1}{\Delta_{a-}^2} \right) \\ &\approx \frac{\Gamma_{1,2}(g_C - g_L)^2g_a^2}{(\Delta_a^2 - \delta^2 - (g_C - g_L)^2)^2}.\end{aligned}\quad (\text{D3})$$

We see that the coupler isolates the qubit from dissipation on the next-to-nearest-neighbor coupler transmon to fourth order in $g_C - g_L, g_a/\Delta_a$. Although $\Gamma_{1,a}$ turns off at $g_C - g_L = 0$, it is difficult to achieve sizeable “on” Γ_a values using the coupler in dispersive operation. This weak “on” interaction motivates the alternative approach taken in the main text.

4. Energy relaxation into the flux-bias line

A critical consideration for choosing an appropriate mutual inductance between the coupler SQUID and its flux

bias line is the relaxation rate of the coupler induced due to this inductive coupling. This relaxation can lead to strong correlations if $\delta \ll |g_C - g_L|$. In this circumstance the “bright” state is the one that tunes strongly with flux and will relax, at worst, at the sum of the individual transmon relaxation rates. In the other regime $\delta \gg |g_C - g_L|$, the eigenstates $|\pm\rangle$ are closely approximated by independent transmon eigenstates, such that we can approximately map $\xi_j \leftrightarrow \xi_{\pm}$ for $j \in \{1, 2\}$. Assuming $\dot{\Phi}_e = M\dot{I}$, this allows us to write the effective decay rate as,

$$\begin{aligned}\Gamma_{1,\pm}^{\text{FB}} &\sim \left(\frac{\xi_{\pm}(\Phi_e)M}{\Phi_0} \right)^2 S_{jj}(\omega) \\ &= \frac{2\hbar\xi_{\pm}^2(\Phi_e)M^2\omega_{\pm}^3}{\Phi_0^2Z_0},\end{aligned}\quad (\text{D4})$$

where in the first line we use the flux participation ratio as prescribed by the third line of Eq. (A6), and in the second line we assume that the magnitude of current fluctuations is set by their vacuum expectation value, i.e., $S_{jj}(\omega) = \omega_{\pm}^2 S_{jj}(\omega) = 2\hbar\omega_{\pm}^3/Z_0$.

Given a mutual inductance $M = 3.7$ pH, capacitive coupling $C_{12} \ll C_1, C_2$, dimensionless coupling constant

$$\begin{aligned}\xi_{\pm}(0) &\sim (\Phi_0/\sqrt{2\hbar Z_1})E'_{12}(0)/E'_1(0), \\ &\text{or } (\Phi_0/\sqrt{2\hbar Z_2})E'_{12}(0)/E'_2(0),\end{aligned}$$

transition frequency $\omega_{\pm}/2\pi = 5$ GHz, and bath impedance of 50 Ω , the equation above leads to an estimated $\Gamma_{1,\pm}^{\text{FB}} \sim 1 \times 10^3 \text{ s}^{-1}$, before additional low-pass filtering of the flux bias. We note that these are worst-case calculations since $\xi_{\pm}(\Phi_e) \propto \cos(2\pi\Phi_e/\Phi_0)$, which at $\Phi_e^{(0)} \sim 0.25\Phi_0$ causes the dimensionless coupling constant $\xi(\Phi_e)$ to vanish.

-
- [1] A. Cross in *APS March Meeting Abstracts*, Vol. 2018 (2018), p. L58.
 - [2] F. Arute, K. Arya, R. Babbush, D. Bacon, J. C. Bardin, R. Barends, R. Biswas, S. Boixo, F. G. Brandao, and D. A. Buell, *et al.*, Quantum supremacy using a programmable superconducting processor, *Nature* **574**, 505 (2019).
 - [3] M. Gong, S. Wang, C. Zha, M.-C. Chen, H.-L. Huang, Y. Wu, Q. Zhu, Y. Zhao, S. Li, and S. Guo, *et al.*, Quantum walks on a programmable two-dimensional 62-qubit superconducting processor, *Science* **372**, 948 (2021).
 - [4] G. Q. AI, Exponential suppression of bit or phase errors with cyclic error correction, *Nature* **595**, 383 (2021).
 - [5] Y. Wu, W.-S. Bao, S. Cao, F. Chen, M.-C. Chen, X. Chen, T.-H. Chung, H. Deng, Y. Du, and D. Fan, *et al.*, Strong Quantum Computational Advantage Using a Superconducting Quantum Processor, *Phys. Rev. Lett.* **127**, 180501 (2021).
 - [6] A. O. Niskanen, Y. Nakamura, and J.-S. Tsai, Tunable coupling scheme for flux qubits at the optimal point, *Phys. Rev. B* **73**, 094506 (2006).

- [7] A. O. Niskanen, K. Harrabi, F. Yoshihara, Y. Nakamura, S. Lloyd, and J. S. Tsai, Quantum coherent tunable coupling of superconducting qubits, *Science* **316**, 723 (2007).
- [8] M. S. Allman, J. D. Whittaker, M. Castellanos-Beltran, K. Cicak, F. da Silva, M. P. DeFeo, F. Lecocq, A. Sirois, J. D. Teufel, J. Aumentado, and R. W. Simmonds, Tunable Resonant and Nonresonant Interactions Between a Phase Qubit and *lc* Resonator, *Phys. Rev. Lett.* **112**, 123601 (2014).
- [9] J. D. Whittaker, F. C. S. da Silva, M. S. Allman, F. Lecocq, K. Cicak, A. J. Sirois, J. D. Teufel, J. Aumentado, and R. W. Simmonds, Tunable-cavity QED with phase qubits, *Phys. Rev. B* **90**, 024513 (2014).
- [10] R. C. Bialczak, M. Ansmann, M. Hofheinz, M. Lenander, E. Lucero, M. Neeley, A. D. O’Connell, D. Sank, H. Wang, M. Weides, J. Wenner, T. Yamamoto, A. N. Cleland, and J. M. Martinis, Fast Tunable Coupler for Superconducting Qubits, *Phys. Rev. Lett.* **106**, 060501 (2011).
- [11] Y. Chen, *et al.*, Qubit Architecture with High Coherence and Fast Tunable Coupling, *Phys. Rev. Lett.* **113**, 220502 (2014).
- [12] M. R. Geller, E. Donate, Y. Chen, M. T. Fang, N. Leung, C. Neill, P. Roushan, and J. M. Martinis, Tunable coupler for superconducting xmon qubits: Perturbative nonlinear model, *Phys. Rev. A* **92**, 012320 (2015).
- [13] P. Roushan, C. Neill, A. Megrant, Y. Chen, R. Babbush, R. Barends, B. Campbell, Z. Chen, B. Chiaro, and A. Dunsworth, *et al.*, Chiral ground-state currents of interacting photons in a synthetic magnetic field, *Nat. Phys.* **13**, 146 (2016).
- [14] C. Neill, *et al.*, A blueprint for demonstrating quantum supremacy with superconducting qubits, *Science* **360**, 195 (2018).
- [15] T. Noh, Z. Xiao, K. Cicak, X. Y. Jin, E. Doucet, J. Teufel, J. Aumentado, L. C. G. Govia, L. Ranzani, A. Kamal, and R. W. Simmonds, Strong parametric dispersive shifts in a statically decoupled multi-qubit cavity QED system, *ArXiv:2103.09277* (2021).
- [16] F. Yan, P. Krantz, Y. Sung, M. Kjaergaard, D. L. Campbell, T. P. Orlando, S. Gustavsson, and W. D. Oliver, Tunable Coupling Scheme for Implementing High-Fidelity Two-Qubit Gates, *Phys. Rev. Appl.* **10**, 054062 (2018).
- [17] Y. Sung, L. Ding, J. Braumüller, A. Vepsäläinen, B. Kannan, M. Kjaergaard, A. Greene, G. O. Samach, C. McNally, D. Kim, A. Melville, B. M. Niedzielski, M. E. Schwartz, J. L. Yoder, T. P. Orlando, S. Gustavsson, and W. D. Oliver, Realization of High-Fidelity CZ and ZZ-Free *i*SWAP Gates with a Tunable Coupler, *Phys. Rev. X* **11**, 021058 (2021).
- [18] X. Li, T. Cai, H. Yan, Z. Wang, X. Pan, Y. Ma, W. Cai, J. Han, Z. Hua, X. Han, Y. Wu, H. Zhang, H. Wang, Y. Song, L. Duan, and L. Sun, Tunable Coupler for Realizing a Controlled-Phase Gate with Dynamically Decoupled Regime in a Superconducting Circuit, *Phys. Rev. Appl.* **14**, 024070 (2020).
- [19] M. C. Collodo, J. Herrmann, N. Lacroix, C. K. Andersen, A. Remm, S. Lazar, J.-C. Besse, T. Walter, A. Wallraff, and C. Eichler, Implementation of Conditional Phase Gates Based on Tunable *zz* Interactions, *Phys. Rev. Lett.* **125**, 240502 (2020).
- [20] Y. Xu, J. Chu, J. Yuan, J. Qiu, Y. Zhou, L. Zhang, X. Tan, Y. Yu, S. Liu, J. Li, F. Yan, and D. Yu, High-Fidelity, High-Scalability Two-Qubit Gate Scheme for Superconducting Qubits, *Phys. Rev. Lett.* **125**, 240503 (2020).
- [21] J. Stehlik, D. M. Zajac, D. L. Underwood, T. Phung, J. Blair, S. Carnevale, D. Klaus, G. A. Keefe, A. Carniol, M. Kumph, and *et al.*, Tunable Coupling Architecture for Fixed-Frequency Transmon Superconducting Qubits, *Phys. Rev. Lett.* **127**, 080505 (2021).
- [22] E. A. Sete, A. Q. Chen, R. Manenti, S. Kulshreshtha, and S. Poletto, Floating Tunable Coupler for Scalable Quantum Computing Architectures, *Phys. Rev. Appl.* **15**, 064063 (2021).
- [23] F. Marxer, *et al.*, Long-Distance Transmon Coupler with CZ-Gate Fidelity above 99.8%, *PRX Quantum* **4**, 010314 (2023).
- [24] A. Kandala, K. X. Wei, S. Srinivasan, E. Magesan, S. Carnevale, G. Keefe, D. Klaus, O. Dial, and D. McKay, Demonstration of a High-Fidelity CNOT Gate for Fixed-Frequency Transmons with Engineered ZZ Suppression, *Phys. Rev. Lett.* **127**, 130501 (2021).
- [25] I. N. Moskalenko, I. A. Simakov, N. N. Abramov, A. A. Grigorev, D. O. Moskalev, A. A. Pishchimova, N. S. Smirnov, E. V. Zikiy, I. A. Rodionov, and I. S. Besedin, High fidelity two-qubit gates on fluxoniums using a tunable coupler, *npj Quantum Inf.* **8**, 130 (2022).
- [26] P. Zhao, Y. Zhang, G. Xue, Y. Jin, and H. Yu, Tunable coupling of widely separated superconducting qubits: A possible application toward a modular quantum device, *Appl. Phys. Lett.* **121**, 032601 (2022).
- [27] E. Zakka-Bajjani, F. Nguyen, M. Lee, L. R. Vale, R. W. Simmonds, and J. Aumentado, Quantum superposition of a single microwave photon in two different “colour” states, *Nat. Phys.* **7**, 599 (2011).
- [28] J.-C. Besse, K. Reuer, M. C. Collodo, A. Wulff, L. Wernli, A. Copetudo, D. Malz, P. Magnard, A. Akin, M. Gabureac, G. J. Norris, J. I. Cirac, A. Wallraff, and C. Eichler, Realizing a deterministic source of multipartite-entangled photonic qubits, *Nat. Commun.* **11**, 4877 (2020).
- [29] D. C. McKay, S. Filipp, A. Mezzacapo, E. Magesan, J. M. Chow, and J. M. Gambetta, Universal Gate for Fixed-Frequency Qubits via a Tunable Bus, *Phys. Rev. Appl.* **6**, 064007 (2016).
- [30] R. K. Naik, N. Leung, S. Chakram, P. Groszkowski, Y. Lu, N. Earnest, D. C. McKay, J. Koch, and D. I. Schuster, Random access quantum information processors using multimode circuit quantum electrodynamics, *Nat. Commun.* **8**, 1904 (2017).
- [31] J. D. Strand, M. Ware, F. Beaudoin, T. A. Ohki, B. R. Johnson, A. Blais, and B. L. T. Plourde, First-order sideband transitions with flux-driven asymmetric transmon qubits, *Phys. Rev. B* **87**, 220505 (2013).
- [32] E. A. Sete, N. Didier, A. Q. Chen, S. Kulshreshtha, R. Manenti, and S. Poletto, Parametric-Resonance Entangling Gates with a Tunable Coupler, *Phys. Rev. Appl.* **16**, 024050 (2021).
- [33] M. Reagor, C. B. Osborn, N. Tezak, A. Staley, G. Prawiroatmodjo, M. Scheer, N. Alidoust, E. A. Sete, N. Didier, M. P. da Silva, and *et al.*, Demonstration of universal parametric entangling gates on a multi-qubit lattice, *Sci. Adv.* **4**, eaao3603 (2018).
- [34] S. A. Caldwell, N. Didier, C. A. Ryan, E. A. Sete, A. Hudson, P. Karalekas, R. Manenti, M. P. da Silva, R. Sinclair,

- and E. Acala, *et al.*, Parametrically Activated Entangling Gates using Transmon Qubits, *Phys. Rev. Appl.* **10**, 034050 (2018).
- [35] J. Majer, J. M. Chow, J. M. Gambetta, J. Koch, B. R. Johnson, J. A. Schreier, L. Frunzio, D. I. Schuster, A. A. Houck, and A. Wallraff, *et al.*, Coupling superconducting qubits via a cavity bus, *Nature* **449**, 443 (2007).
- [36] J. M. Chow, J. M. Gambetta, A. W. Cross, S. T. Merkel, C. Rigetti, and M. Steffen, Microwave-activated conditional-phase gate for superconducting qubits, *New J. Phys.* **15**, 115012 (2013).
- [37] H. Goto, Double-Transmon Coupler: Fast Two-Qubit Gate with No Residual Coupling for Highly Detuned Superconducting Qubits, *Phys. Rev. Appl.* **18**, 034038 (2022).
- [38] K. Kubo and H. Goto, Fast parametric two-qubit gate for highly detuned fixed frequency superconducting qubits using a double-transmon coupler, *Appl. Phys. Lett.* **122**, 064001 (2023).
- [39] J. Koch, T. M. Yu, J. Gambetta, A. A. Houck, D. I. Schuster, J. Majer, A. Blais, M. H. Devoret, S. M. Girvin, and R. J. Schoelkopf, Charge-insensitive qubit design derived from the Cooper pair box, *Phys. Rev. A* **76**, 042319 (2007).
- [40] P. Krantz, M. Kjaergaard, F. Yan, T. P. Orlando, S. Gustavsson, and W. D. Oliver, A quantum engineer's guide to superconducting qubits, *Appl. Phys. Rev.* **6**, 021318 (2019).
- [41] P. Mundada, G. Zhang, T. Hazard, and A. Houck, Suppression of Qubit Crosstalk in a Tunable Coupling Superconducting Circuit, *Phys. Rev. Appl.* **12**, 054023 (2019).
- [42] A. Kandala, K. X. Wei, S. Srinivasan, E. Magesan, S. Carnevale, G. A. Keefe, D. Klaus, O. Dial, and D. C. McKay, Demonstration of a High-Fidelity CNOT Gate for Fixed-Frequency Transmons with Engineered ZZ Suppression, *Phys. Rev. Lett.* **127**, 130501 (2021).
- [43] J. Ku, X. Xu, M. Brink, D. C. McKay, J. B. Hertzberg, M. H. Ansari, and B. L. T. Plourde, Suppression of Unwanted ZZ Interactions in a Hybrid Two-Qubit System, *Phys. Rev. Lett.* **125**, 200504 (2020).
- [44] J. M. Gambetta, A. A. Houck, and A. Blais, Superconducting Qubit with Purcell Protection and Tunable Coupling, *Phys. Rev. Lett.* **106**, 030502 (2011).
- [45] F. Yan, S. Gustavsson, A. Kamal, J. Birenbaum, A. P. Sears, D. Hover, T. J. Gudmundsen, D. Rosenberg, G. Samach, and S. Weber, *et al.*, The flux qubit revisited to enhance coherence and reproducibility, *Nat. Commun.* **7**, 12964 (2016).
- [46] B. Kannan, A. Almanakly, Y. Sung, A. Di Paolo, D. A. Rower, J. Braumüller, A. Melville, B. M. Niedzielski, A. Karamlou, K. Serniak, A. Vepsäläinen, M. E. Schwartz, J. L. Yoder, R. Winik, J. I.-J. Wang, T. P. Orlando, S. Gustavsson, J. A. Grover, and W. D. Oliver, On-demand directional microwave photon emission using waveguide quantum electrodynamics, *Nat. Phys.* **19**, 394 (2023).
- [47] Z. Xiao, E. Doucet, T. Noh, L. Ranzani, R. Simmonds, L. Govia, and A. Kamal, Perturbative Diagonalization for Time-Dependent Strong Interactions, *Phys. Rev. Appl.* **18**, 024009 (2022).
- [48] J. Braumüller, L. Ding, A. P. Vepsäläinen, Y. Sung, M. Kjaergaard, T. Menke, R. Winik, D. Kim, B. M. Niedzielski, and A. Melville, *et al.*, Characterizing and Optimizing Qubit Coherence Based on SQUID Geometry, *Phys. Rev. Appl.* **13**, 054079 (2020).
- [49] E. Kiktenko, A. Nikolaeva, P. Xu, G. Shlyapnikov, and A. Fedorov, Scalable quantum computing with qudits on a graph, *Phys. Rev. A* **101**, 022304 (2020).
- [50] J. M. Baker, C. Duckering, and F. T. Chong, in *2020 IEEE 50th International Symposium on Multiple-Valued Logic (ISMVL)* (IEEE, Miyazaki, Japan, 2020), p. 303.
- [51] R.-P. Riwar and D. P. DiVincenzo, Circuit quantization with time-dependent magnetic fields for realistic geometries, *npj Quantum Inf.* **8**, 36 (2022).
- [52] U. Vool and M. Devoret, Introduction to quantum electromagnetic circuits, *Int. J. Circuit Theory Appl.* **45**, 897 (2017).
- [53] X. You, J. A. Sauls, and J. Koch, Circuit quantization in the presence of time-dependent external flux, *Phys. Rev. B* **99**, 174512 (2019).
- [54] J. Johansson, P. Nation, and F. Nori, QuTiP: An open-source Python framework for the dynamics of open quantum systems, *Comput. Phys. Commun.* **183**, 1760 (2012).
- [55] J. Johansson, P. Nation, and F. Nori, QuTiP 2: A Python framework for the dynamics of open quantum systems, *Comput. Phys. Commun.* **184**, 1234 (2013).
- [56] A. Altland and B. D. Simons, *Condensed Matter Field Theory* (Cambridge University Press, Cambridge, UK, 2010), 2nd ed.